이학박사학위논문

Optimizing the Properties of Large-Area Graphene for High-Performance Transparent Electrodes

대면적 그래핀의 특성 최적화 및 고성능 투명전극 응용

2015년 8월

서울대학교 대학원

화학부 물리화학 전공

김 상 진

Ph. D. Thesis

Optimizing the Properties of Large-Area Graphene for High-Performance Transparent Electrodes

Supervisor: Professor Byung Hee Hong

Major: Physical Chemistry

By Sang Jin Kim

Department of Chemistry

Graduate School of Seoul National University

2015

Abstract

In chapter 1, briefly introduce the 2D materials that have been intensively studied as emerging materials for future electronics, including flexible electronics, photonics, and electrochemical energy storage devices. Among representative 2D materials (such as graphene, boron nitride, and transition metal dichalcogenides) that exhibit extraordinary properties, graphene stands out in the flexible electronics field due to its combination of high electron mobility, high thermal conductivity, high specific surface area, high optical transparency, excellent mechanical flexibility, and environmental stability.

Cu catalyst etching is one of the key processes to produce large-area graphene through chemical vapor deposition (CVD), which is needed to remove Cu catalysts and transfer graphene onto target substrates for further applications. Chapter 2 introduce that the addition of metal-chelating agents such as benzimidazole (BI) to etching solution. The resulting graphene film prepared by Cu stabilizing agent exhibits a low sheet resistance without additional doping processes. It also confirmed that such strong doping effect is stable enough to last for more than 10 months under ambient conditions due to the barrier properties of graphene.

Chapter 3 introduce an ultraclean, cost-effective, and easily scalable method of transferring and patterning graphene using pressure sensitive adhesive films (PSAFs) at room temperature. This transfer is enabled by the difference in wettability and adhesion energy of graphene with respect to

PSAF and a target substrate. The PSAF transferred graphene is found to be free from residues, and shows excellent charge carrier mobility with less doping effect compared to the other polymer supported methods. In addition, the sheet resistance of graphene transferred by recycled PSAF does not change considerably up to 4 times.

Chapter 4 introduce the 0-dimensional graphene quantum dots (GQDs) that have been widely exploited due to tunable optical and electronic properties. Moreover, the dispersibility of GQDs can be controlled by chemical functionalization. A surface-engineered GQD in hole extraction polymer photovoltaic device shows enhanced power conversion efficiency (PCE) leading to significantly improved short circuit current density (Jsc) value. To maximize the PCE of the device, hydrophobic reduced GQDs were additionally incorporated in a bulk-heterojunction layer, which is found to promote a synergistic effect with the GQD-incorporated hole extraction layer.

Keyword : graphene, graphene quantum dots, chemical doping, pressure sensitive adhesive films, transparent electrodes, Organic photovoltaics

Student Number : 2012-30871

Table of Contents

List of Figures

Chapter 1

Chapter 2

transferred graphene on a SiO_2/Si wafer and a PET substrate, respectively. Scale bars, 1 cm.

Figure 2-3. (**a-b**) X-Ray photoelectron spectroscopy (XPS) spectra of BI-graphene, showing clear C 1s and N 1s (inset) peaks that indicate the existence of nitrogen-containing BI molecules. (**c**) UV-Vis. absorption spectra of different etching solutions with and without BI. (**d**) UV-Vis absorption spectra of the BI-added etching solution with increasing reaction time. The absorption in longer wavelength is originated from a charge transfer complex between Cu^{2+} and ammonia/sulfate. The peak intensity in the shorter wavelength range increases as the added BI molecules form a complex with oxidized Cu ions.

Figure 2-4. (**a**) Raman spectra (excitation wavelength: 514nm) of the BI-graphene film on a SiO_2/Si substrate, compared with APS-etched graphene. (**b**) An AFM image of CVD graphene on SiO_2/Si, showing the clean surface without dopant residues. (**c**) A TEM image of graphene on a lacey carbon grid. (**d**) An EDS analysis of graphene. (**e**) A selected area electron diffraction (SAED) pattern of graphene. (**f**) A high resolution TEM image of graphene.

Figure 2-5. (**a**) Sheet resistance mapping of a large-area BI-graphene film transferred on a PET substrate by roll-to-roll (R2R) processes. (**b**) Relative sheet resistance change of BI-graphene prepared by simultaneous etching and doping, compared to post-doped graphene by $HAuCl_4$ solution (black, Ref 35) with respect to exposure time at ambient condition for more than 10 months. (**c**) FET characteristics of the APS- and BI-graphene (V_{SD}= 0.01V), indicating the strong p-doping after BI-etching. (scale bar = 20μm)

Figure 2-6. Sheet resistances of BI-graphene films with increasing number of layers under ambient conditions (red) and a standard durability test condition (85% humidity at 85°C, blue), in comparison with APS–etched graphene (black) and dually BI- doped graphene (cyan).

Figure 2-7. Optical transmittance at 550 nm of graphene films with increasing number of layers. Each graphene layer absorbs ~2.7% of light, which is slightly higher than 2.3% of pristine graphene due to the residual BI molecules after simultaneous etching and doping.

Figure 2-8. (**a**) FET characteristics of BI-graphene with different concentration of BI in etchants. (**b**) FET characteristics of APS-graphene (black), APS-graphene spin-coated with BI (red), and APS-graphene dipped in BI etchant (blue) for 1 hr. V_{sd}= 10 mV. The FET device structure is illustrated in the inset. This result indicates that the strong p-doping effect of BI is available only when dissolved in H_2O_2:H_2SO_4 solution.

Chapter 3

Figure 3-1. The relative adhesive force of supporting polymer layers measured by contact mode AFM. (**a**) PSAF and (**b**) PMMA supporting layers show relatively weak adhesive force of 15.6 nN and 17.4 nN, respectively. However, the adhesive force of TRT could not measured owing to the large adhesion property of TRT. The adhesive force was measured by contact mode AFM (Park System, XE-100) with catilever (MikroMasch HQ:CSC38).

Figure 3-2. **Schematic representation for PMMA and PSAF-assisted transfer processes.** (a) A wet-transfer process using PMMA supporting layer. The morphology of the PMMA layers is rigid and reverse to the rough surface of Cu. The unmatched morphologies between PMMA and target surfaces (incomplete wetting) result in occurrence of ripples and tears during the dissolution of PMMA. (b) A dry transfer using PSAF includes the complete wetting step, where the liquid-like PSA layer adapts its morphology to target surface as soft pressure applied on it.

Figure 3-3. Comparison between PMMA, TRT and PSAF-transferred graphene. (a, b) SEM and AFM images of as-grown graphene on Cu, showing periodic steps of Cu. (c, d) OM and AFM images of PMMA-transferred graphene on SiO_2, showing PMMA residues and ripples reversely templated by Cu steps. (e, f) OM and AFM images of TRT-transferred graphene on SiO_2. The large thermal deformation of the release and target films at the temperature close to their T_g (glass transition temperature) resulted in the occurrence of ripples on polymer residues. (g, h) OM and AFM images of PSAF-transferred graphene on SiO_2, showing ultraclean surface without residues and periodic ripples. The thick ripples originate from the negative thermal expansion of graphene.

Figure 3-4. Characteristics of PSAF-transferred graphene compared with TRT and PMMA- transferred graphene. (a) Raman spectra of graphene films transferred on SiO_2/Si substrates (excitation wavenumber, 514nm). (b) G and 2D band shift of graphene, indicating that the PSAF-transferred graphene is much less p-doped. (c) FET characteristics of graphene films on SiO_2/Si substrates (V_{sd}= 10 mV). (d) Mobility distribution of graphene FET devices. Average carrier mobility of PSAF, PMMA and TRT-transferred graphene are ~5,300 $cm^2/V \cdot s$, ~1,500 $cm^2/V \cdot s$, and ~1,000 $cm^2/V \cdot s$, respectively.

Figure 3-5. XPS spectra of graphene transferred by PSAFs, PMMA and TRT film, respectively. XPS analyses were carried out using Thermo Scientific K-Alpha (small-spot X-ray Photoelectron Spectrometer system)

Figure 3-6. PSAF-assisted transfer of large-area graphene films on various substrates. (a-d) Graphene on a 4-inch wafer, a B5-sized PET film,

PEDOT:PSS films without GQDs (A) and incorporating GQDs (B), which were spin coated on top of the ITO glass. Spherical aberration corrected transmission electron microscopy (Cs-corrected TEM) images of PEDOT:PSS film without (C) and with (D) GQDs. GQD concentration was 0.4 wt %.

Figure 4-5. (A) AFM images of the PEDOT:PSS layer without GQDs, and with various ratios of GQDs: (B) 0.2, (C) 0.4 and (D) 0.6.

Figure 4-6. Schematic of chemical structures of PEDOT, PSS and GQD.

Figure 4-7. Line measurement results of the surface morphology of the bare PEDOT:PSS film (A)~(C), and the GQD-incorporated PEDOT:PSS film (D)~(F). The average values of the estimated grain size were around 30 nm for the bare PEDOT:PSS, and around 70 nm for the GQD-incorporated PEDOT:PSS. The line measurement was conducted using SPM Lab Analysis software (Veeco instruments, Inc.)

Figure 4-8. Device performance and characterization. Current vs. potential (J-V) curves (A), and incident photon-to-charge-carrier-efficiency (IPCE) and IPCE enhancement factor for the devices (B). Nyquist plots of electrochemical impedance spectroscopy at 0.55 V (C) and at open circuit potential (D). 0.4 wt. % of GQDs was incorporated into PEDOT:PSS layer.

Figure 4-9. UV- visible adsorption spectra of GQDs in methanol solvent (A). UV-visible adsorption spectra (B) and diffuse reflectance spectra (C) of 40nm-thick PEDOT:PSS films coated on ITO glass. Reflectance spectra of full device structural samples (ITO/PEDOT:PSS/BHJ/TiO_x/Al) where from 700 nm to 750 nm is a lamp changing region (D). 0.4 wt % of GQDs were incorporated into PEDOT:PSS layer.

Figure 4-10. Optical simulation of E-field intensity distribution of GQD obtained by the finite difference time domain (FDTD) method at 500nm (A). (B) and (C) show optical simulation of a gold nanoparticle with the same shape and size as GQDs at 500nm and 600nm respectively.

Figure 4-11. Cyclic voltammetry (CV) curves (scanning rate of 50 mV/s) of GQDs deposited on a platinum (Pt) sheet in acetonitrile solution with 0.1M tetrabutylammonium hexafluorophosphate as an electrolyte. Pt foil and Ag/AgCl were used as the counter and the reference electrodes. GQD solutions were drop-cast on the Pt sheet and fully dried to prepare the working electrode.

Figure 4-12. AFM and device performance in comparison with rGQD and GQDs in PEDOT:PSS. AFM images of PEDOT:PSS films incorporating 0.05 wt% of rGQDs (A) and 0.4 wt% of GQDs (B).Current vs. potential (J-V) curves (C), and incident photon-to-charge-carrier-efficiency (IPCE) (D) for

List of Tables

Chapter 3

Chapter 4

Chapter 1. General Introduction†

† This is reproduced from Sang Jin Kim, Kyoungjun Choi, Bora Lee, Yuna Kim, and Byung Hee Hong, *Annu. Rev. Mater. Res.* **2015**. 45: 16.1-16.22 © 2015 by Annual Reviews.

1.1. Abstract

Recently, 2D materials have been intensively studied as emerging materials for future electronics, including flexible electronics, photonics, and electrochemical energy storage devices. Among representative 2D materials (such as graphene, boron nitride, and transition metal dichalcogenides) that exhibit extraordinary properties, graphene stands out in the flexible electronics field due to its combination of high electron mobility, high thermal conductivity, high specific surface area, high optical transparency, excellent mechanical flexibility, and environmental stability. This review covers the synthesis, transfer, and characterization methods of graphene and 2D materials and graphene's application to flexible devices as well as comparison with other competing materials.

1.2. Introduction

Future electronics technology will evolve from rigid devices to bendable/rollable/foldable devices that are wearable like clothes or accessories (Figure 1-1) (1). These flexible devices will be advantageous over rigid ones due to their better durability, lighter weight, higher space efficiency, and improved comfort, but the development of such devices requires breakthroughs in materials because they will require flexibility as well as desirable electrical insulating/semiconducting/metallic properties. Traditional device fabrication processes have been limited mostly to rigid substrates and vacuum deposition methods. However, recently emerging 2D materials such as graphene, boron nitride (BN), and transition metal dichalcogenides (TMDCs) are attractive because of their outstanding electrical, optical, and mechanical properties, which are ideal for flexible and stretchable electronics.

Graphene not only exhibits excellent optoelectronic and mechanical properties but also can exhibit good adhesion with several organic materials so as to produce high-performance organic field-effect transistors (FETs), organic light-emitting diodes (OLEDs), and organic photovoltaic cells (OPVs). The high specific surface-to-volume ratio of graphene and its excellent chemical stability are also expected to be useful for higher-performance power storage devices by optimizing chemical functionalization and doping processes. However, the etching methods used to remove graphene from catalytic substrates and its transfer will be as important as the synthesis of high-quality, large-area, defect-free material by chemical vapor deposition (CVD). Through these processes, the overall quality of graphene can be

optimized to be used for flexible electronics, as reviewed below.

Figure 1-1. Progress toward industrial applications of flexible electronics. (a) Future flexible devices will come from the fabrication of bendable, rollable, or foldable structures. (b) A graphene-based capacitive touch-screen device showing high flexibility and transparency.

1.3. Methods for Graphene Synthesis and Transfer

In 2004, Geim's group at Manchester University first succeeded in isolating single-layer graphene from graphite (Figure 1-2a) (2). 3D graphite consisted of many layers of 2D graphene by weak van der Waals bonding. In principle, each monolayer graphene sheet can be isolated from the surface of a highly oriented pyrolytic graphite flake by using an adhesive tape. A multiple-peeling process leads to monolayer graphene. The so-called mechanical exfoliation method provides a highly crystalline structure of graphene with outstanding electrical properties such as the ambipolar field effect (2), the quantum Hall effect at room temperature (3-7), and extremely high carrier mobility for fundamental studies (8, 9). However, this method is limited by the size of the graphite flakes available (typically micrometer in size). Furthermore, the thickness is difficult to accurately control, resulting in a low-yield problem, and so this is an unsuitable technique for mass production.

Ruoff's group demonstrated a solution-based process for obtaining single-layer graphene by chemical exfoliation (Figure 1-2b) (10-13). The chemical exfoliation method uses strong acids and oxidants to obtain a sheet of graphene oxide (GO) from graphite powder dispersed in solution. This method can introduce structural and electrical disorder in the graphene during the oxidation process, and so an additional process was needed to enhance the electrical property of GO due to oxygen-rich functional groups on GO's surface. Reduced graphene oxide (RGO) films have good conducting properties, which can be obtained by treating GO films with reducing agents

such as hydrazine or hydrothermal annealing. Although chemical exfoliation is a simple, solution-based process and can produce large quantities of graphene at low cost, the electrical and optical properties of RGO films are inferior to those of the graphene film obtained by mechanical exfoliation or CVD methods.

The epitaxial growth process is another possible method that allows for the production of high-quality and large-area single layers and multilayers of graphene on silicon carbide (SiC) (0001) in high vacuum and high temperature (~1,000–1,600^{o}C). In this process, Si is sublimated, leaving carbon behind (Figure 1-2c) (14-16) on the surface of the SiC. SiC wafers can be utilized as a substrate for graphene electronic devices because SiC is a wide-band-gap material but is rigid. Although graphene grown by the epitaxial process has outstanding electrical properties, enabling it to be utilized in high-frequency (~100-GHz) electrical devices (17), SiC substrates are relatively expensive and limited in size. It is also difficult to transfer graphene grown in this way onto other arbitrary substrates for commercial adoption.

Graphene has also been grown by the thermal chemical vapor deposition (T-CVD) method, which consists of decomposition of hot hydrocarbon sources on catalytic surfaces or surface segregation of carbon during a cooling step from the carbon/metal binary phase system. Carbon sources, such as CH_4, C_2H_2, or solid sources [polystyrene, polyacrylonitrile, polymethyl methacrylate (PMMA) polymers], and various transition metal catalysts (Cu, Ni, Pd, Ru, Ir, or alloys) have been used for graphene growth by

T-CVD (18-27). Growth conditions such as the temperature dependence of carbon solubility in the metal and the gas flow rate and pressure determine the morphology (domain size and boundaries) and quality of graphene films grown by the T-CVD method.

In 2009, our group reported the growth of graphene on polycrystalline Ni thin films and showed high electron mobility [up to 3,650 $cm^2/(V•s)$ of carrier mobility] (Figure 1-2d) (24). However, graphene grown on Ni thin films consists of a mixture of both single layers and multilayers because the thickness control of graphene on a Ni surface depends on the rapid cooling condition of the metal carbide state. Due to the very low carbon solubility in Cu, the Cu catalyst is favored to obtain high-quality, uniform, and single-layer-dominant (>95%) graphene. The scale of graphene grown on Cu ranges from 30 inches (28) to 100 m (29). Unfortunately, the T-CVD process requires very high temperatures (>1,000 ^oC) and is not suitable for mass production. Plasma-assisted CVD methods overcome this limitation of T-CVD by using combined thermal and plasma energy, which facilitates the decomposition of hydrocarbon at lower temperatures (<1,000 ^oC) (30-33). The electrical and optical properties of graphene films grown using plasma-assisted CVD were controlled by varying the plasma power, growth time, and growth temperature.

A graphene film is extremely thin and easy to tear during the catalyst etching and transfer processes. Therefore, to reduce defects produced during the transfer process to a suitable target substrate, as-grown graphene films need a polymer supporting layer. One method, the wet-transfer method, uses

spin-coated PMMA or polydimethylsiloxane (PDMS) as a supporting and protective layer (34). In contrast, in dry-transfer methods, the use of thermal release tape allows for large-area graphene transfer onto flexible polymers and rigid substrates without being limited in size (28, 35). Multiple stacking methods are also used to enhance the electrical conductivity of graphene films through the layer-by-layer printing process (36-38). Refinement of direct deposition and transfer methods of graphene onto insulating substrates will be key to replacing indium tin oxide (ITO) as the ubiquitous transparent conductor (39-41).

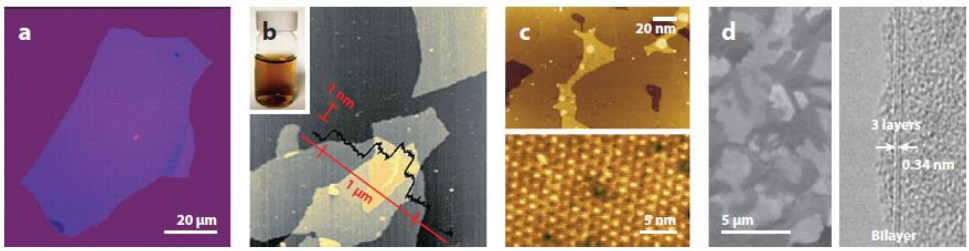

Figure 1-2. Graphene films produced by various methods. (*a*) Photograph of a multilayer graphene flake isolated from bulk graphite by using the mechanical exfoliation method with adhesive tape. (*b*) AFM image of graphite oxide sheets deposited onto a mica substrate from an aqueous dispersion (*inset*) obtained by the chemical exfoliation method. (*c*) STM topographs of epitaxial graphene on silicon carbide (SiC) (0001) show large flatness. (*d*) SEM (*left*) and TEM (*right*) images of graphene films on Ni layers grown by the chemical vapor deposition method.

1.4. Optimizing Properties for Flexible and Stretchable devices

Graphene has a unique band structure that results in many attractive electronic properties, such as a 10–100-times-higher carrier mobility than Si. For instance, in 2008, Kim's group at Columbia showed that single-layer graphene prepared by using the mechanical exfoliation method exhibited carrier mobility in excess of 200,000 $cm^2/(V•s)$ at room temperature (Figure 1-3a) (42). By fabricating a suspended graphene channel, they were able to minimize substrate-induced scattering and to obtain essentially ballistic charge transport at millimeter length scales at room temperature.

Lee et al. (43) reported that single-layer graphene is mechanically very strong. They showed that when a graphene sheet suspended across 1.0-1.5-μm cavities in a SiO2 film was deflected using an AFM tip, the graphene sheet stayed intact (43) and exhibited a Young's modulus of 1 TPa and a large spring constant (1-5 N/m) (Figure 1-3b). The excellent mechanical properties of graphene have also been investigated by measuring the electrical resistance on stretching, and as shown in Figure 1-3c (24), the resistance shows little variation with strain. This combination of large strain capability and small changes in resistance is necessary for the operation durability of a flexible and stretchable device.

Presently, ITO is widely used as a transparent conductor for optoelectronic devices. However, ITO has poor mechanical properties; it tends to crack easily or shows defects when strained. For these reasons, the use of graphene has been widely investigated in recent years as a transparent

conductor for optoelectronic and photonic applications because of its combination of electrical, mechanical, and optical properties. The optical properties of graphene result in high opacity for an atomic monolayer. The transmittance of graphene decreases approximately 2.3% with each layer as the number of graphene layers increases (Figure 1-3d) (44). Furthermore, graphene films transferred onto flexible polyethylene terephthalate (PET) and stretchable PDMS substrates maintain their high transparency and flexible properties (34).

The adsorption of various molecules on the graphene surface is possible because of graphene's hydrophobic surface, which is similar to that of carbon nanotubes (CNTs). Also, the conductivity and doping types can be modified by chemical treatment. There are now numerous reports of doping methods such as modification of the substrate surface with self-assembled monolayers (45, 46); sp^3 functionalization of carbon with H, F, or Cl (47); atomic substitution with N (48, 49); and surface treatment of graphene by using certain molecules (50-52) or acidic solutions (37).

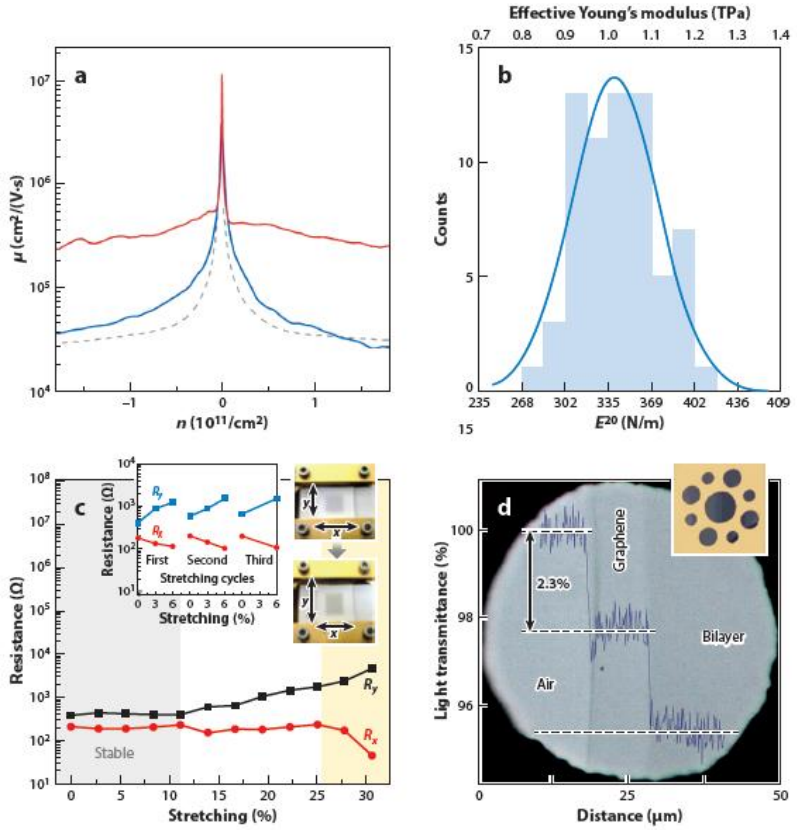

Figure 1-3. The outstanding properties of graphene for flexible electronics. (*a*) Mobility as a function of carrier density of a suspended graphene device shows its high electron mobility [~200,000 $cm^2/(V \cdot s)$]. (*b*) Elastic stiffness distribution of graphene film on a silicon oxide cavity. (*c*) The resistance change of a graphene film transferred onto a polydimethylsiloxane substrate depends on isotropic stretching. (*Insets*) The resistance change and movement images depend on stretching cycles and stretching direction. (*d*) Transmittance of partially covered single-layer and bilayer graphene. The inset shows the metal support structure covered with graphene layers.

1.5. References

1. Ahn, J.-H.; Hong, B.H. *Nat. Nanotechnol.* **2014**, *9*, 737-738.

2. Novoselov, K.S.; Geim, A.K.; Morozov, S.V.; Jiang, D.; Zhang, Y. et al. *Science* **2004**, *306*, 666-669.

3. Novoselov, K.S.; McCann, E.; Morozov, S.V.; Fal'ko, V.I.; Katsnelson, M.I. et al. *Nat. Phys.* **2006**, *2*, 177-180.

4. Jiang, Z.; Zhang, Y.; Tan, Y.W.; Stormer, H.L.; Kim, P. *Solid State Commun*. **2007**, *143*, 14-19.

5. Jiang, Z.; Zhang, Y.; Stormer, H.L.; Kim, P. *Phys. Rev. Lett.* **2007**, *99*, 106802.

6. Zhang, Y.; Tan, Y.-W.; Stormer, H.L.; Kim, P. *Nature* **2005,** *438*, 201-204.

7. Novoselov, K.S.; Jiang, Z.; Zhang, Y.; Morozov, S.V.; Stormer, H.L.; et al. *Science* **2007**, *315*, 1379.

8. Geim, A.K.; Novoselov, K.S. *Nat. Mater.* **2007**, *6*, 183-191.

9. Katsnelson, M.I. *Mater. Today* **2007,** *10*, 20-27.

10. Stankovich, S.; Dikin, D.A.; Dommett, G.H.B.; Kohlhaas, K.M.; Zimney, E.J.; et al. *Nature* **2006**, *442*, 282-286.

11. Stankovich, S.; Dikin, D.A.; Piner. R.D.; Kohlhaas, K.A.; Kleinhammes, A. et al. *Carbon* **2007**. *45*, 1558-1565.

12. Jung, I.; Dikin, D.A.; Piner, R.D.; Ruoff, R.S. *Nano Lett.* **2008**, *8*, 4283-4287.

13. Yang, D.; Velamakanni, A.; Bozoklu, G.; Park, S.; Stoller, M. et al. *Carbon* **2009**, *47*, 145-152.

14. Berger, C.; Song, Z.; Li, X.; Wu, X.; Brown, N. et al. *Science* **2006**. *312*, 1191-1196.

15. de Heer, W.A.; Berger, C.; Wu, X.; First, P.N.; Conrad, E.H. et al. *Solid State Commun.* **2007**, *143*, 92-100.

16. Hass, J.; de Heer, W.A.; Conrad, E.H. *J. Phys. Condens. Matter* **2008**, *20*, 323202.

17. Lin, Y.-M.; Dimitrakopoulos, C.; Jenkins, K.A.; Farmer, D.B.; Chiu, H.-Y. et al. *Science* **2010**, *327*, 662.

18. Sun, Z.; Yan, Z.; Yao, J.; Beitler, E.; Zhu, Y.; Tour, J.M. *Nature* **2010**, *468*, 549-552.

19. Byun, S.-J.; Lim, H.; Shin, G.-Y.; Han, T.-H.; Oh, S.H. et al. *Phys. Chem. Lett.* **2011**, *2*, 493-497.

20. Li, X.; Cai, W.; An, J.; Kim, S.; Nah, J. et al. *Science* **2009**, *324*, 1312-1314.

21. Kwon, S.-Y.; Ciobanu, C.V.; Petrova, V.; Shenoy, V.B.; Bareño, J. et al. *Nano Lett.* **2009**, *9*, 3985-3990.

22. Sutter, P.W.; Flege, J.-I.; Sutter, E.A. *Nat. Mater.* **2008**, *7*, 406-411.

23. Coraux, J.; N'Diaye, A.T.; Busse, C.; Michely, T. *Nano Lett.* **2008**, *8*, 565-570.

24. Kim, K.S.; Zhao, Y.; Jang, H.; Lee, S.Y.; Kim, J.M. et al. *Nature* **2009**, *457*, 706-710.

25. Shin, H.-A.-S.; Ryu, J.; Cho, S.-P.; Lee, E.-K.; Cho, S. et al. *Phys. Chem. Chem. Phys.* **2014**, *16*, 3087-3094.

26. Dai, B.; Fu, L.; Zou, Z.; Wang, M.; Xu, H. et al. *Nat. Commun.* **2011**, *2*, 522.

27. Chen, S.; Brown, L.; Levendorf, M.; Cai, W.; Ju, S.-Y. et al. *ACS Nano* **2011**, *5*, 1321-1327.

28. Bae, S.; Kim, H.; Lee, Y.; Xu, X.; Park, J.-S. et al. *Nat. Nanotechnol*. **2010**, *5*, 574-578.

29. Kobayashi, T.; Bando, M.; Kimura, N.; Shimizu, K.; Kadono, K. et al. *Appl. Phys. Lett.* **2013**, *102*, 023112.

30. Malesevic, A.; Vitchev, R.; Schouteden, K.; Volodin, A.; Zhang, L. et al. *Nanotechnology* **2008**, *19*, 305604.

31. Malesevic, A.; Kemps, R.; Vanhulsel, A.; Chowdhury, M.P.; Volodin, A.; Van Haesendonck, C. *J. Appl. Phys*. **2008**, *104*, 084301.

32. Shang, N.G.; Papakonstantinou, P.; McMullan, M.; Chu, M.; Stamboulis, A. et al. *Adv. Funct. Mater.* **2008**, *18*, 3506-3514.

33. Kim, Y.-J.; Kim, S.J.; Jung, M.H.; Choi, K.Y.; Bae, S. et al. *Nanotechnology* **2012**, *23*, 344016.

34. Lee, Y.; Bae, S.; Jang, H.; Jang, S.; Zhu, S.-E. et al. *Nano Lett.* **2010**, *10*, 490-493.

35. Kang, J.; Hwang, S.; Kim, J.H.; Kim, M.H.; Ryu, J. et al. *ACS Nano* **2012,** *6*, 5360-5365.

36. Güneş, F.; Shin, H.-J.; Biswas, C.; Han, G.H.; Kim, E.S. et al. *ACS Nano* **2010,** *4*, 4595-4600.

37. Kasry, A.; Kuroda, M.A.; Martyna, G.J.; Tulevski, G.S.; Bol, A.A. *ACS Nano* **2010**, *4*, 3839-3844.

38. Li, X.; Zhu, Y.; Cai, W.; Borysiak, M.; Han, B. et al. *Nano Lett.* **2009**, *9*, 4359-4363.

39. Ismach, A.; Druzgalski, C.; Penwell, S.; Schwartzberg, A.; Zheng, M. et al. *Nano Lett.* **2010**, *10*, 1542-1548.

40. Bi, H.; Sun, S.; Huang, F.; Xie, X.; Jiang, M. *J. Mater. Chem.* **2012,** *22*, 411-416.

41. Kim, H.; Song, I.; Park, C.; Son, M.; Hong, M. et al. *ACS Nano* **2013**, *7*, 6575-6582.

42. Bolotin, K.I.; Sikes, K.J.; Jiang, Z.; Klima, M.; Fudenberg, G. et al. *Solid State Commun.* **2008**, *146*, 351-355.

43. Lee, C.; Wei, X.; Kysar, J.W.; Hone, J. *Science* **2008**, *321*, 385-388.

44. Nair, R.R.; Blake, P.; Grigorenko, A.N.; Novoselov, K.S.; Booth, T.J. et al. *Science* **2008**, *320*, 1308.

45. Park, J.; Lee, W.H.; Huh, S.; Sim, S.H.; Kim, S.B. et al. *J. Phys. Chem. Lett.* **2011**, *2*, 841-845.

46. Park, J.; Jo, S.B.; Yu, Y.-J.; Kim, Y.; Yang, J.W. et al. *Adv. Mater.* **2012**, *24*, 407-411.

47. Wu, J.; Xie, L.; Li, Y.; Wang, H.; Ouyang, Y. et al. *J. Am. Chem. Soc.* **2011**, *133*, 19668-19671.

48. Guo, B.; Liu, Q.; Chen, E.; Zhu, H.; Fang, L.; Gong, J.R. *Nano Lett.* **2010**, *10*, 4975-4980.

49. Wei, D.; Liu, Y.; Wang, Y.; Zhang, H.; Huang, L.; Yu, G. *Nano Lett.* **2009**, *9*, 1752-1758.

50. Chen, W.; Chen, S.; Qi, D.C.; Gao, X.Y.; Wee, A.T.S. *J. Am. Chem. Soc.* **2007**, *129*, 10418-10422.

51. Medina, H.; Lin, Y.-C.; Obergfell, D.; Chiu, P.-W. *Adv. Funct. Mater.* **2011**, *21*, 2687-2692.

52. Kim, S.J.; Ryu, J.; Son, S.; Yoo, J.M.; Park, J.B. et al. *Chem. Mater.* **2014**, *26*, 2332-2336.

Chapter 2. Optimization by Chemical Doping.

- Simultaneous Etching and Doping by Cu-Stabilizing Agent for High-Performance Graphene-Based Transparent Electrodes [†]

[†] This is reproduced from Sang Jin Kim, Jaechul Ryu, Suyeon Son, Je Min Yoo, Jong Bo Park, Dongkwan Won, Eun-Kyu Lee, Sung-Pyo Cho, Sukang Bae, Seungmin Cho, and Byung Hee Hong, *Chem. Mater.* **2014**. 26 (7) 2332-2336 © American Chemical Society

2.1. Abstract

Cu etching is one of the key processes to produce large-area graphene through chemical vapor deposition (CVD), which is needed to remove Cu catalysts and transfer graphene onto target substrates for further applications. However, the Cu etching method has been much less studied compared to doping or transfer processes despite its importance in producing higher quality graphene films. The Cu etchant generally includes a strong oxidizing agent that converts metallic Cu to Cu^{2+} in a short period of time. Sometimes, the highly concentrated Cu^{2+} causes a side reaction leading to defect formation on graphene, which needs to be suppressed for higher graphene quality. Here we report that the addition of metal-chelating agents such as benzimidazole (BI) to etching solution reduces the reactivity of Cu-etching solution by forming a coordination compound between BI and Cu^{2+}. The resulting graphene film prepared by Cu stabilizing agent exhibits a sheet resistance as lows as ~200 Ohm/sq. without additional doping processes. We also confirmed that such strong doping effect is stable enough to last for more than 10 months under ambient conditions due to the barrier properties of graphene covering the BI dopants, in contrast to the poor stability of graphene additionally doped by strong p-dopant such as $HAuCl_4$. Thus, we expect that this simultaneous doping and etching method would be very useful for simple and high-throughput production of large-area graphene electrodes with enhanced conductivity.

2.2. Introduction

Graphene has outstanding optical,[1] mechanical,[2,3] thermal,[4] and electrical[5-8] properties, which is particularly advantageous for transparent electrode applications. However, its sheet resistance higher than indium tin oxide (ITO) has been a critical problem to hinder the applications of graphene films as transparent electrodes. To overcome such issue, researchers have endeavored to modulate synthesis, etching, and doping processes to obtain enhanced electrical properties of graphene. In recent years, a number of doping methods have been developed which include the modification of substrate surface with self-assembled monolayers (SAM),[9,10] sp^3-functionalization of carbon with H, F or Cl,[11] atomic substitution with N,[12,13] and surface treatment of graphene using certain molecules[10,14-17] or acidic solutions.[18] However, these additional doping processes often result in unexpected structural defects or inhomogeneous charge distribution on graphene, which deteriorated the electrical property of graphene films. In particular, the doping effect from acidic solution treatment[18] or molecule adsorption[10,14-17] decreases with time due to the instability and volatility of doping agents under ambient conditions[19] Herein, we report a novel Cu etching method of using Cu^{2+}-chelating agent such as benzimidazole (BI) that is capable of forming a coordination compound with Cu^{2+}. The BI is well known as a heterocyclic molecular with strong electron affinity and excellent chemical and thermal stability.[20-23] Thus, it strongly p-dopes graphene without any additional process.[24] Finally, the resulting graphene (BI-graphene)

showed excellent sheet resistance as lows as ~200 ohm/sq. and high carrier concentration ($n=\sim 1.0 \times 10^{13}$ cm^{-2}) mainly due to the strong electron withdrawing property of the BI molecules. In addition, the overlying impermeable graphene layer[25,26] protects the BI molecules from reactive environments. As a result, the high electrical properties of BI-graphene can be stably maintained not only at an ambient condition but also at a rigorous durability test condition such as 85% humidity at 85°C.

2.3. Experimental Section

*Graphene synthesis and etchant preparation***.** Graphene was synthesized by chemical vapor deposition (CVD) method on a high purity copper foil (Alpha Aecer, 99.999%) with flowing 3 sccm H_2 and 30 sccm CH_4 gases at 1,000℃. After coating a PMMA polymer layer on one side of as-grown Cu foil, the graphene on the other side was removed by oxygen plasma. The Cu foil was etched in H_2SO_4 : H_2O_2 : H_2O solution with a volume ratio of 1: 3: 20. Additionally, ammonium persulfate (APS) and benzimidazole (BI) powders were added to make 0.03 M and 0.06 M solutions, respectively. After rinsing with distilled water, the graphene was transferred on target substrates. The sample was finally soaked in acetone to remove the PMMA layer.

Device fabrication. First, chrome (5nm) and gold (30nm) electrodes were deposited on a SiO_2 (300nm)/Si^{++} wafer by thermal evaporation, and graphene was transferred on top of the electrodes, followed by pattering by oxygen plasma using photolithography.

*Characterization***.** The Raman spectra were obtained by a Raman spectrometer (RM 1000-Invia, Renishaw, 514nm). The optical transmittance of graphene was measured using an ultraviolet-visible spectrometer (UV-3600, Shimazdu). The AFM image was measured by a noncontact mode (Park System, XE-100). XPS analyses were carried out using Thermo Scientific K-Alpha (small-spot X-ray Photoelectron Spectrometer system). The TEM images were obtained with a JEOL JEM- 3010 electron microscope operating at 300 kV. The sheet resistance was measured with 4-point probe nanovoltmeter (Keithley 6221),

and the current-voltage curve was measured by Agilent B2912A. The absorbance of etching solutions was measured by Scinco s-3100 spectrophotometer.

2.4. Results and Discussion

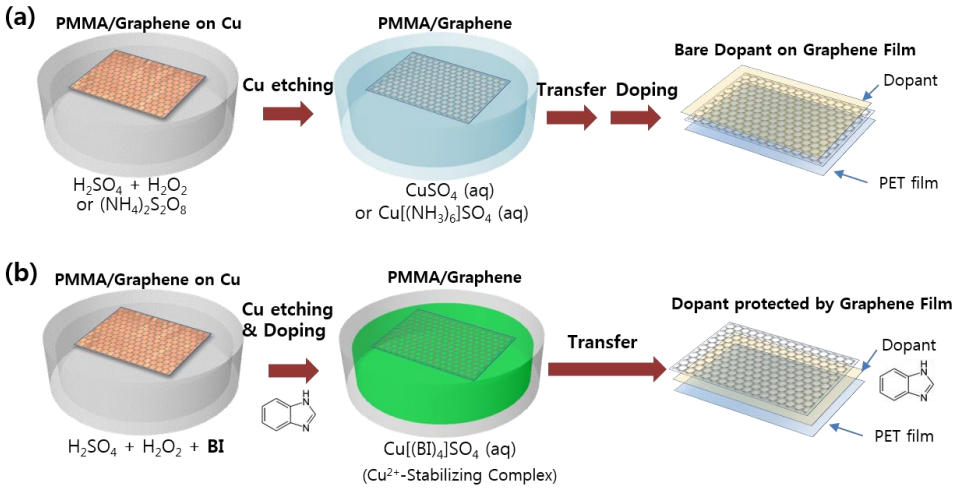

Figure 2-1. Comparison between sequential and simultaneous Cu-etching and doping processes for graphene synthesized on Cu by chemical vapor deposition. (**a**) A schematic representation for the sequential etching and doping processes without BI. (**b**) A schematic representation for the simultaneous etching and doping processes with BI, where the Cu-stabilizing complexes are formed to prevent the rigorous reaction between Cu and etching solution. Please note that the dopant molecules in (b) are sandwiched between graphene and PET substrates, while the dopant in (a) is exposed to air without protection layers, which is important for long-term stability of the doping effect.

Figure 2-1 illustrates the schematic representation of sequential and simultaneous Cu-etching and doping processes for graphene synthesized on Cu by chemical vapor deposition (CVD) method. The polymethyl-methacrylate (PMMA) coated graphene-Cu samples were floated on H_2SO_4 + H_2O_2 or $(NH_4)_2S_4O_8$ (ammonium persulfate: APS) and simultaneous etching solution with Cu stabilizing agent (H_2SO_4 + H_2O_2 + BI) to confirm the effect of etching solution on graphene. The preparation of the BI-graphene needs

only 2 steps excluding an additional doping process, while the conventional method requires 3~4 steps to complete the doping of graphene. During the etching process, highly concentrated Cu^{2+} can catalyze a reaction that forms undesirable defects on graphene.[27] Such catalytic activity of Cu^{2+} ions can be suppressed by adding metal-chelating agents such as BI as it readily forms a coordination compound, $Cu[(BI)_4]SO_4(aq)$, during the etching process.[28] The transferred BI-graphene on arbitrary substrates such as SiO_2/Si wafers and PET films were shown in figure 2-2.

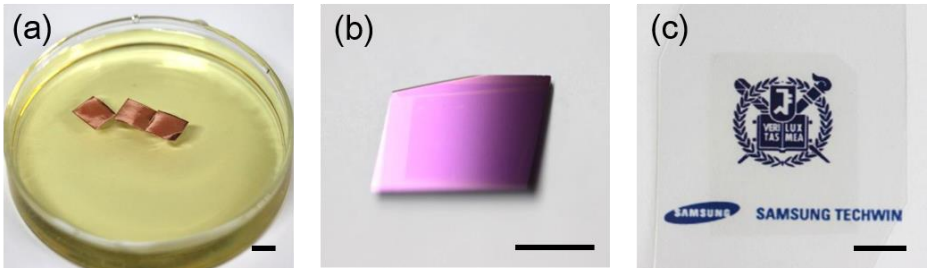

Figure 2-2. (**a**) A Photograph of the as-synthesized graphene film on Cu substrates, floating on a Cu-stabilizing etchant solution. (**b, c**) Photographs of transferred graphene on a SiO_2/Si wafer and a PET substrate, respectively. Scale bars, 1 cm.

Figure 2-3a shows the spectra of X-ray photoelectron spectroscopy (XPS) of BI-graphene on a SiO_2/Si substrate, which confirms the existence of carbon, oxygen, and nitrogen bonding states corresponding to BI and graphene.[29,30] The C 1s peak indicates that a certain degree of oxidation is occurred during the synthesis and etching processes. It can be further decomposed into C sp^2, C-OH, C-O-C, C=O and C-N peaks at 284.3, 284.9, 285.9, 287.7 and 285.3 eV, respectively (Figure 2b). The strong N1s peak

clearly shows that considerable amount of BI molecules are sandwiched between the overlying graphene layer and underneath substrates (Figure 2-3b, inset). Figure 2-3c displays UV-Vis. absorption spectra of different etching solutions with and without BI, indicating that the yellowish color comes from the weak charge-transfer complex between BI and Cu ion.

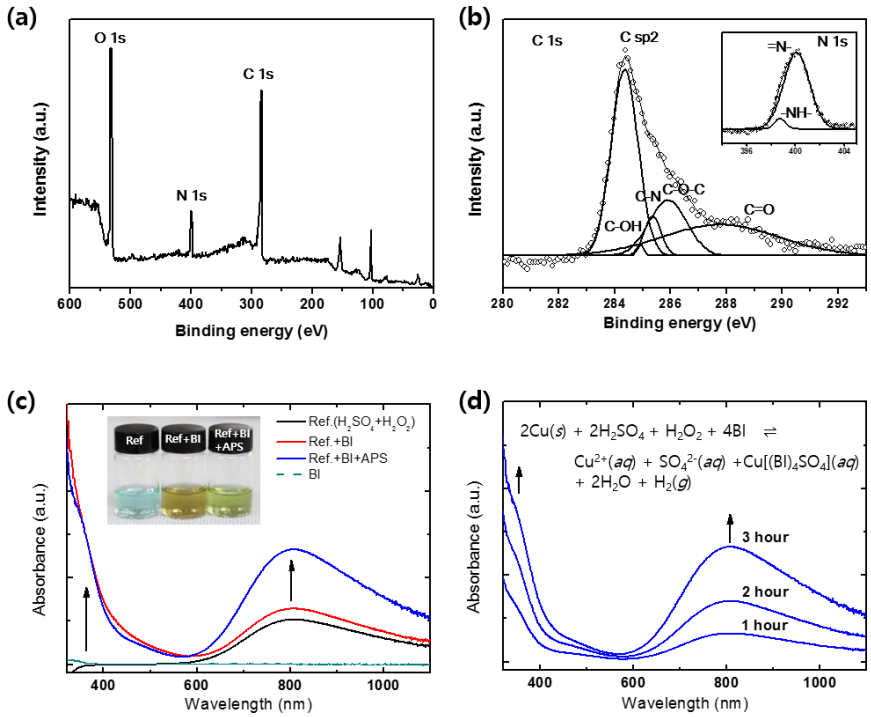

Figure 2-3. (**a-b**) X-Ray photoelectron spectroscopy (XPS) spectra of BI-graphene, showing clear C 1s and N 1s (inset) peaks that indicate the existence of nitrogen-containing BI molecules. (**c**) UV-Vis. absorption spectra of different etching solutions with and without BI. (**d**) UV-Vis absorption spectra of the BI-added etching solution with increasing reaction time. The absorption in longer wavelength is originated from a charge transfer complex between Cu^{2+} and ammonia/sulfate. The peak intensity in the shorter wavelength range increases as the added BI molecules form a complex with oxidized Cu ions.

The inset photo also shows clearly different colors of each etching solution, depending on metal chelating species. The peak intensity increases with Cu etching time as the concentration of Cu^{2+} increases (Figure 2d).

Figure 2-4a shows the Raman spectra of BI-graphene films on a SiO_2/Si substrate. Compared to the graphene film etched in an ammonium persulfate (APS) solution (APS-graphene), the BI-graphene exhibits stronger p-doping effect due to the residual BI molecules that withdraw electrons from graphene. The intensity of the D band was negligibly small for both APS-graphene and BI-graphene. However, the spectral background for BI-graphene near the D band region was slightly increased due to BI.[31] In addition, the 2D and G bands were slightly up-shifted, and the I(2D)/I(G) ratio was significantly decreased, which indicates the stronger p-doping effect by BI. On the other hand, the APS etching resulted in mild p-doping of graphene.[32] The atomic force microscope (AFM) image was taken to confirm the clean surface of BI-graphene (Figure 2-4b).

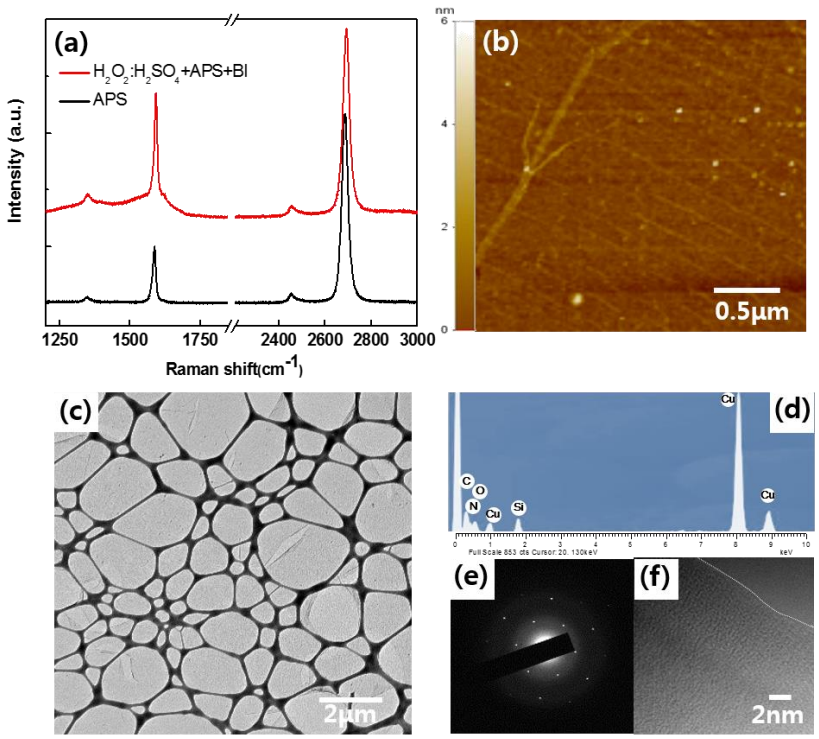

Figure 2-4. (**a**) Raman spectra (excitation wavelength: 514nm) of the BI-graphene film on a SiO_2/Si substrate, compared with APS-etched graphene. (**b**) An AFM image of CVD graphene on SiO_2/Si, showing the clean surface without dopant residues. (**c**) A TEM image of graphene on a lacey carbon grid. (**d**) An EDS analysis of graphene. (**e**) A selected area electron diffraction (SAED) pattern of graphene. (**f**) A high resolution TEM image of graphene.

A transmission electron microscope (TEM) image (Figure 2-4c,f) and its selected area electron diffraction (SAED) pattern (Figure 2-4e) show the highly crystalline hexagonal structures of BI-graphene. Based on the nitrogen composition from energy dispersive X-ray spectroscopy (EDS) analysis, we could confirm that BI molecules are well distributed on the graphene surface. We could further infer that BI adsorption on the graphene surface is not responsible for defect formation.

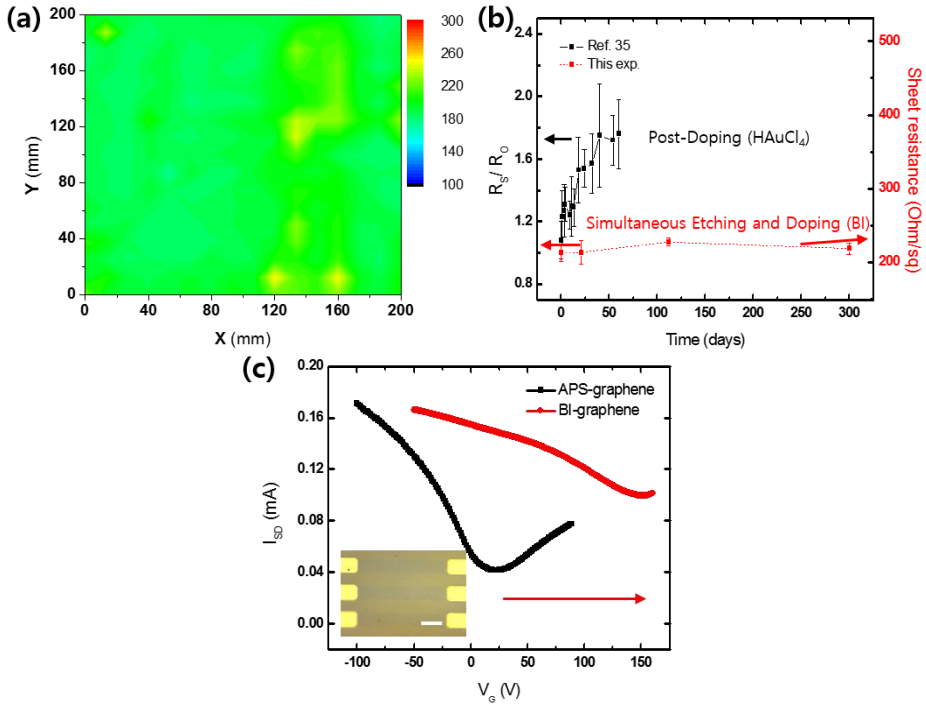

Figure 2-5. (**a**) Sheet resistance mapping of a large-area BI-graphene film transferred on a PET substrate by roll-to-roll (R2R) processes. (**b**) Relative sheet resistance change of BI-graphene prepared by simultaneous etching and doping, compared to post-doped graphene by $HAuCl_4$ solution (black, Ref 35) with respect to exposure time at ambient condition for more than 10 months. (**c**) FET characteristics of the APS- and BI-graphene (V_{SD}= 0.01V), indicating the strong p-doping after BI-etching. (scale bar = 20μm)

Figure 2-5a shows the sheet resistance mapping of a large-area BI-graphene film transferred on a PET substrate by roll-to-roll (R2R) processes.[33] The sheet resistance of BI-graphene is as lows as ~200 Ohm/sq, and shows less than 10 % variation over 200 x 200 mm^2 area, indicating that the BI molecules are uniformly adsorbed on graphene surface. In addition, the BI-graphene shows an outstanding stability for more than 10 months under ambient conditions (Figure 2-5b), which is attributed to the outstanding impermeability of graphene that protects BI from reactive environments.[24,25,35]

The comparison between BI-graphene and APS-graphene clearly shows the strong p-doping effect that lowers the sheet resistance by more than 44% (figure 2-6).

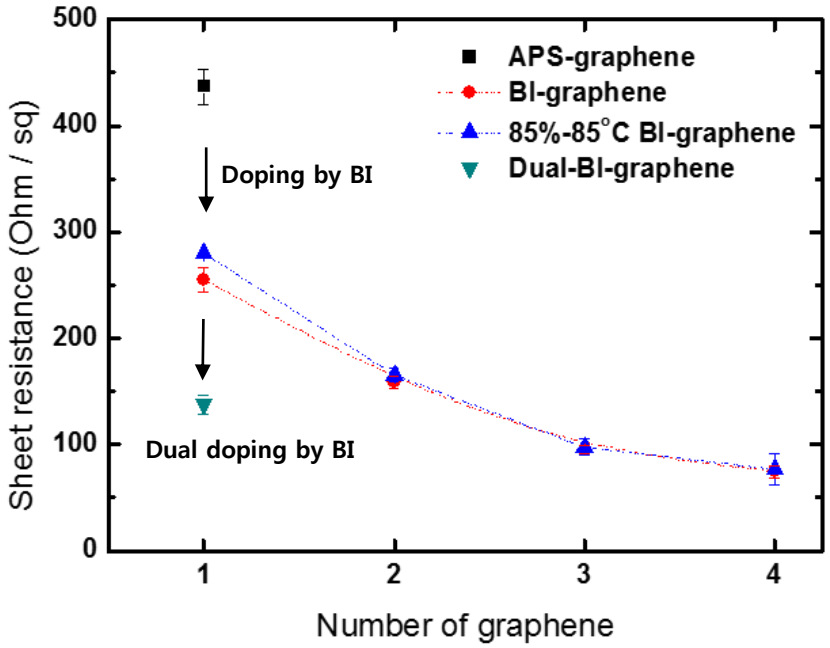

Figure 2-6. Sheet resistances of BI-graphene films with increasing number of layers under ambient conditions (red) and a standard durability test condition (85% humidity at 85°C, blue), in comparison with APS–etched graphene (black) and dually BI- doped graphene (cyan).

Moreover, the sheet resistance of dually BI-doped graphene showed ~137 Ohm/sq, which is 70 % lower than that of APS-graphene. As the number of BI-graphene layers increases, the sheet resistance gradually decreases. Even when BI-graphene was exposed to relatively harsh condition – 85 %

humidity and 85 ºC temperature – for 24 hours, it maintained outstanding stability. Each BI-graphene layer absorbs ~2.7% of light, which is slightly higher than 2.3% of pristine graphene due to the residual BI molecules after simultaneous etching and doping (figure 2-7).

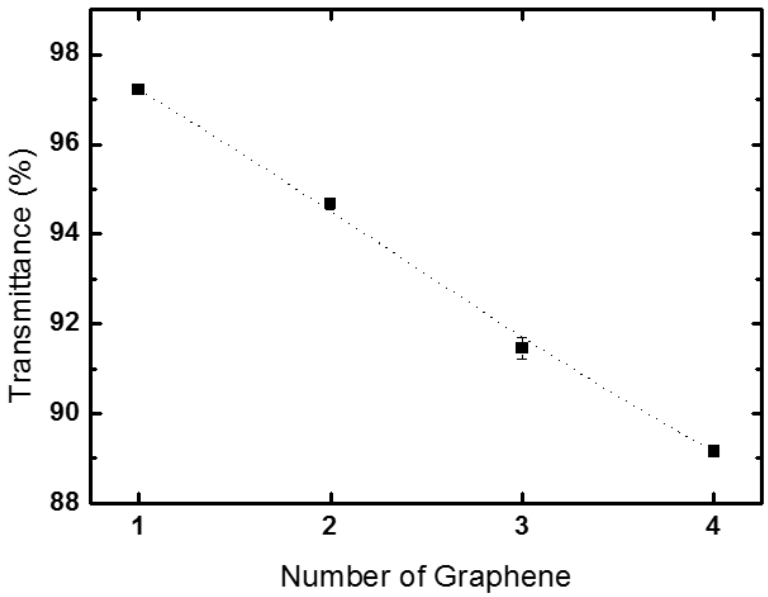

Figure 2-7. Optical transmittance at 550 nm of graphene films with increasing number of layers. Each graphene layer absorbs ~2.7% of light, which is slightly higher than 2.3% of pristine graphene due to the residual BI molecules after simultaneous etching and doping.

The field effect transistors (FET) characteristics of the BI-graphene exhibits stronger p-doping effect than APS-graphene, showing Dirac voltage of ~146 V (n= 1 x 10^{13} cm^{-2}) and carrier (hole) mobility of ~1153 $cm^2/(V \cdot s)$ owing to the unique electron withdrawing property of BI.[34] The charge neutral voltages of FET were up-shifted with respect to the increasing BI

concentration in etchants, which yielded p-doping effect (figure 2-8a).. The comparison between the FET characteristics of APS-graphene, APS-graphene spin-coated with BI, and APS-graphene dipped in BI etchant indicates that the strong p-doping effect of BI is available only when dissolved in H_2O_2-H_2SO_4 etching solution (figure 2-8b).

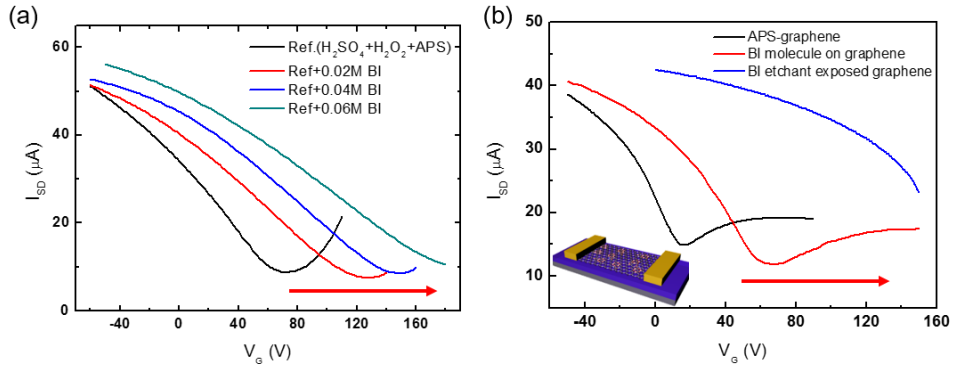

Figure 2-8. (**a**) FET characteristics of BI-graphene with different concentration of BI in etchants. (**b**) FET characteristics of APS-graphene (black), APS-graphene spin-coated with BI (red), and APS-graphene dipped in BI etchant (blue) for 1 hr. V_{sd}= 10 mV. The FET device structure is illustrated in the inset. This result indicates that the strong p-doping effect of BI is available only when dissolved in H_2O_2:H_2SO_4 solution.

2.5. Conclusions

In summary, we have demonstrated the simultaneous etching and doping process of graphene by using Cu-stabilizing agent to enhance the electrical conductivity and stability as transparent conducting films. By adding BI molecules in Cu etchant, the catalytic activity of Cu^{2+} ion was suppressed by forming the coordination complex, $Cu[(BI)_4][SO_4](aq)$. The BI-graphene shows the sheet resistance as lows as 200 Ohm/sq with high carrier concentration ($n= 1 \times 10^{13}$ cm^{-2}) and 10-month long stability at ambient conditions. Thus, we believe that this simultaneous doping and etching method based on Cu^{2+}-stabilizing BI complexes would be very useful for simpler and higher-throughput production of large-area graphene electrodes for various practical applications.

2.6. References

1. Blake, P.; Hill, E. W.; Castro Neto, A. H.; Novoselov, K. S.; Jiang, D.; Yang, R.; Booth, T. J.; Geim, A. K. *Appl. Phys. Lett.* **2007**, 91 (6), 06312

2. Lee, C.; Wei, X.; Kysar, J. W.; Hone, J. *Science* **2008,** *321* (5887), 385-388.

3. Kim, K. S.; Zhao, Y.; Jang, H.; Lee, S. Y.; Kim, J. M.; Kim, K. S.; Ahn, J.-H.; Kim, P.; Choi, J.-Y.; Hong, B. H. *Nature* **2009,** *457* (7230), 706-710.

4. Balandin, A. A. *Nat. Mater.* **2011,** *10* (8), 569-581

5. Tan, Y. W.; Zhang, Y.; Bolotin, K.; Zhao, Y.; Adam, S.; Hwang, E. H.; Das Sarma, S.; Stormer, H. L.; Kim, P. *Phys. Rev. Lett.* **2007,** *99* (24), 246803

6. Morozov, S. V.; Novoselov, K. S.; Katsnelson, M. I.; Schedin, F.; Elias, D. C.; Jaszczak, J. A.; Geim, A. K. *Phys. Rev. Lett.* **2008,** *100* (1), 016602

7. Castro Neto, A. H.; Guinea, F.; Peres, N. M. R.; Novoselov, K. S.; Geim, A. K. *Rev. Mod. Phys.* **2009,** *81* (1), 109-162.

8. Adam, S.; Hwang, E. H.; Galitski, V. M.; Das Sarma, S. *Proc. Natl. Acad. Sci.* **2007,** *104* (47), 18392-18397.

9. Park, J.; Lee, W. H.; Huh, S.; Sim, S. H.; Kim, S. B.; Cho, K.; Hong, B. H.; Kim, K. S. *J. Phys. Chem. Lett.* **2011,** *2* (8), 841-845.

10. Park, J.; Jo, S. B.; Yu, Y.-J.; Kim, Y.; Yang, J. W.; Lee, W. H.; Kim, H. H.; Hong, B. H.; Kim, P.; Cho, K. *et al. Adv. Mater.* **2012,** *24* (3), 407-411.

11. Wu, J.; Xie, L.; Li, Y.; Wang, H.; Ouyang, Y.; Guo, J.; Dai, H. *J. Am. Chem. Soc.* **2011,** *133* (49), 19668-19671.

12. Guo, B.; Liu, Q.; Chen, E.; Zhu, H.; Fang, L.; Gong, J. R. *Nano Lett.* **2010,** *10* (12), 4975-4980.

13. Wei, D.; Liu, Y.; Wang, Y.; Zhang, H.; Huang, L.; Yu, G. *Nano Lett.* **2009,** *9* (5), 1752-1758.

14. Chen, W.; Chen, S.; Qi, D. C.; Gao, X. Y.; Wee, A. T. S. *J. Am. Chem. Soc.* **2007,** *129* (34), 10418-10422.

15. Medina, H.; Lin, Y.-C.; Obergfell, D.; Chiu, P.-W. *Adv. Funct. Mater.* **2011,** *21* (14), 2687-2692.

16. Lee, W. H.; Suk, J. W.; Lee, J.; Hao, Y.; Park, J.; Yang, J. W.; Ha, H.-W.; Murali, S.; Chou, H.; Akinwande, D.; Kim, K. S.; Ruoff, R. S. *ACS Nano* **2012,** *6* (2), 1284-1290.

17. Dong, X.; Fu, D.; Fang, W.; Shi, Y.; Chen, P.; Li, L.-J. *Small* **2009,** *5* (12), 1422-1426.

18. Kasry, A.; Kuroda, M. A.; Martyna, G. J.; Tulevski, G. S.; Bol, A. A. *ACS Nano* **2010,** *4* (7), 3839-3844.

19. Bae, S.; Kim, S. J.; Shin, D.; Ahn, J.-H.; Hong, B. H. *Phys. Scr.* **2012**, *T146*, 014024

20. Walba, H.; Isensee, R. W. *J. Org. Chem.* **1961,** *26* (8), 2789-2791.

21. Bradamente, S.; Pagani, G A. *Pure Appl. Chem.* **1989**, *61* (4), 709

22. Kannan, R.; He, G. S.; Yuan, L.; Xu, F.; Prasad, P. N.; Dombroskie, A. G.; Reinhardt, B. A.; Baur, J. W.; Vaia, R. A.; Tan, L.-S. *Chem. Mat.* **2001,** *13* (5), 1896-1904.

23. Kawahara, M.; Morita, J.; Rikukawa, M.; Sanui, K.; Ogata, N. *Electrochim. Acta* **2000**, *45* (8–9), 1395-1398.

24. Kim, H. H.; Yang, J. W.; Jo, S. B.; Kang, B.; Lee, S. K.; Bong, H.; Lee, G.; Kim, K. S.; Cho, K. *ACS Nano* **2013**, *7* (2), 1155-1162.

25. Bunch, J. S.; Verbridge, S. S.; Alden, J. S.; van der Zande, A. M.; Parpia, J. M.; Craighead, H. G.; McEuen, P. L. *Nano Lett.* **2008,** *8* (8), 2458-2462.

26. Chen, S.; Brown, L.; Levendorf, M.; Cai, W.; Ju, S.-Y.; Edgeworth, J.; Li, X.; Magnuson, C. W.; Velamakanni, A.; Piner, R. D.; Kang, J. *et al*. *ACS Nano* **2011,** *5* (2), 1321-1327.

27. Reymond, S. b.; Cossy, J. *Chem. Rev.* **2008,** *108* (12), 5359-5406.

28. Sieron, L. *Acta Crystallogr. Sect. E.-Struct Rep* **2007,** *63* (2), m579-m580.

29. Jaramillo, A.; D. Spurlock, L.; Young, V.; Brajter-Toth, A. *Analyst* **1999,** *124* (8), 1215-1221.

30. Waltman, R. J.; Pacansky, J.; Bates, C. W. *Chem. Mat.* **1993,** *5* (12), 1799-1804.

31. Suwaiyan, A.; Zwarich, R.; Baig, N. *Journal of Raman Spectroscopy* **1990,** *21* (4), 243-249.

32. DasA; PisanaS; ChakrabortyB; PiscanecS; Saha, S. K.; Waghmare, U. V.; Novoselov, K. S.; Krishnamurthy, H. R.; Geim, A. K.; Ferrari, A. C. *et al*. *Nat. Nanotechnol.* **2008,** *3* (4), 210-215.

33. Bae, S.; Kim, H.; Lee, Y.; Xu, X.; Park, J.-S.; Zheng, Y.; Balakrishnan, J.; Lei, T.; Kim, H.R..; Song, Y. I. *et al*. *Nat. Nanotechnol.* **2010,** *5* (8), 574-578.

34. Pisana, S.; Lazzeri, M.; Casiraghi, C.; Novoselov, K. S.; Geim, A. K.; Ferrari, A. C.; Mauri, F. *Nat. Mater.* **2007,** *6* (3), 198-201

35. Yan, C.; Kim, K.-S.; Lee, S.-K.; Bae, S.-H.; Hong, B. H.; Kim, J.-H.; Lee, H.-J.; Ahn, J.-H. *ACS Nano* **2011**, 6 (3), 2096-2103.

Chapter 3. Optimization by Dry Transfer.

- Ultra-Clean Patterned Transfer of Single-Layer Graphene by Recyclable Pressure Sensitive Adhesive Films †

† This is reproduced from Sang Jin Kim, Teajun Choi, Bora Lee, Sunwoo Lee, Kyoungjun Choi, Jong Bo Park, Je Min Yoo, Yong Seok Choi, Jaechul Ryu, Philip Kim, James Hone, and Byung Hee Hong, *Nano Lett.* **2015**. 15(5) 3236-3240 © American Chemical Society

3.1.Abstract

We report an ultraclean, cost-effective, and easily scalable method of transferring and patterning large-area graphene using pressure sensitive adhesive films (PSAFs) at room temperature. This simple transfer is enabled by the difference in wettability and adhesion energy of graphene with respect to PSAF and a target substrate. The PSAF transferred graphene is found to be free from residues, and shows excellent charge carrier mobility as high as ~17,700 $cm^2/V \cdot s$ with less doping compared to the graphene transferred by thermal release tape (TRT) or poly(methyl methacrylate) (PMMA) as well as good uniformity over large areas. In addition, the sheet resistance of graphene transferred by recycled PSAF does not change considerably up to 4 times, which would be advantageous for more cost-effective and environmentally friendly production of large-area graphene films for practical applications.

3.2. Introduction

In recent years, researchers have endeavored to obtain high-quality large-area graphene by modifying the growth conditions of chemical vapor deposition (CVD) processes. However, even the best quality graphene can be easily degraded during the transfer process mainly because of defects, cracks and residues induced by mechanical deformation. Typically, a polymer is utilized as a supporting layer to support graphene during transfer; [1] commonly used polymers include poly(methyl methacrylate) (PMMA), [2-4] thermal release tapes (TRT), etc. [5-6] However, PMMA leaves residue that causes inhomogeneous doping and degradation of charge carrier mobility. [7-10] TRT requires high processing temperature close to the glass transition temperature (T_g) of polymer substrates, which results in considerable thermal stress on graphene. Polymer-free transfer using rigid frames is not suitable for large-scale transfer.[11-12] Other types of clean transfer methods generally require complicated wet cleaning or annealing processes unfavorable for large-area applications.[13-14] Patterning of graphene is a second essential step for fabrication of various graphene-based devices. However, patterning methods relying on photolithography or e-beam lithography also use resist polymers that are difficult to completely remove after patterning. These resist residues also give rise to inhomogeneous doping and scattering problems similar to PMMA. [15-16] Other patterning methods of using block copolymers or inorganic nanostructures as templates are time-consuming and not easily scalable for large-area devices.[17-21]

Here we report an ultraclean, cost-effective, and easily scalable method of transferring and patterning large-area graphene using pressure sensitive adhesive films (PSAFs) at room temperature. This simple transfer is enabled by the difference in wettability and adhesion energy of graphene with respect to PSAF and a target substrate. The adhesive force of the PSAF layer was carefully optimized by adjusting the ratio between silicon-based adhesive precursors, crosslinkers, and anchorage additives that are commercially available at much lower cost than PMMA or TRT (see Experimental Section for details). PSAF-transferred graphene is found to be free from residues, and shows excellent charge carrier mobility as high as 17,700 $cm^2/V \cdot s$, with less doping compared to TRT and PMMA-transferred graphene, and good uniformity over large areas. In addition, the PSAF is recyclable because it does not need to be dissolved for removal, which is important for cost-effective production of graphene films for practical applications.

3.3. Results and Discussion

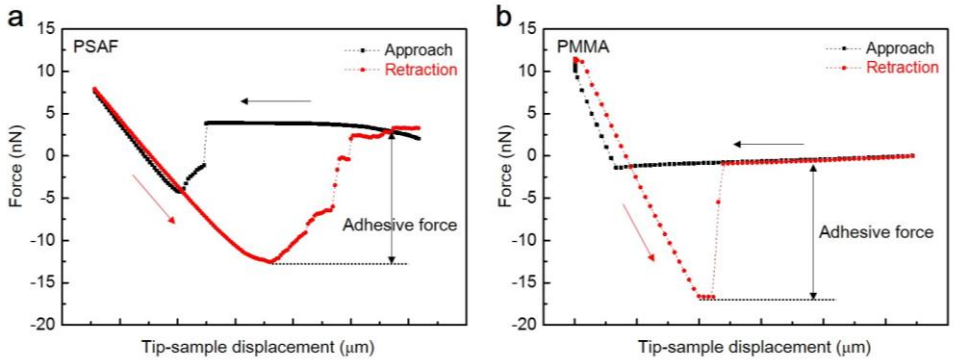

Figure 3-1. The relative adhesive force of supporting polymer layers measured by contact mode AFM. (**a**) PSAF and (**b**) PMMA supporting layers show relatively weak adhesive force of 15.6 nN and 17.4 nN, respectively. However, the adhesive force of TRT could not measured owing to the large adhesion property of TRT. The adhesive force was measured by contact mode AFM (Park System, XE-100) with catilever (MikroMasch HQ:CSC38).

First, a large-area graphene film was synthesized by chemical vapor deposition (CVD) on a high purity copper foil (99.99%) with flowing 3 sccm H_2 (70 mtorr) and 30 sccm CH_4 (340 mtorr) gases at 1,000ºC. After coating or laminating PMMA, TRT, and PSAF layers on the as-grown graphene on the Cu foil, the graphene on the other side was removed by spray etching with 0.1M ammonium persulfate (APS) solution. After completely removing Cu by further etching, the graphene on the supporting polymer layer was rinsed with DI water and transferred onto target substrates. Finally, the supporting PSAF, TRT, and PMMA layers were removed or delaminated from graphene by peeling, hot pressing, or acetone treatment, respectively. Contact mode atomic

force microscopy (AFM) analysis shows that PSAF and PMMA layers have relatively very weak adhesive forces of 15.6 nN and 17.4 nN, respectively (Figure 3-1). The net adhesive force of PSAF is similar to that of PMMA, but the PSAF tends to be detached from the surface gradually owing to its liquid-like behaviors, while the PMMA shows a sudden increase in the force measurement. We suppose that this enables perfect wetting at graphene-PSAF interface and smooth transfer of graphene from PSAF to SiO_2 surface during the peeling-off process.

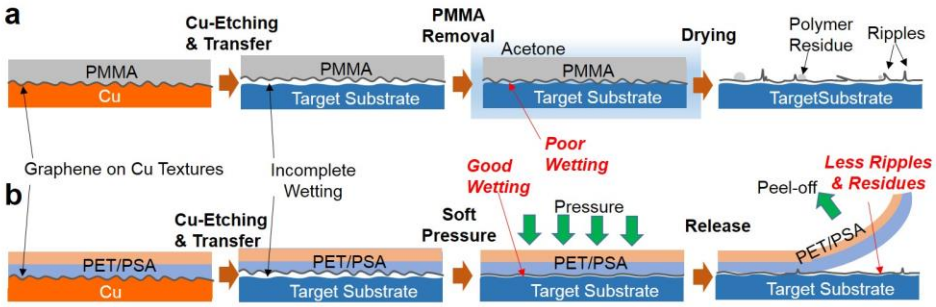

Figure 3-2. Schematic representation for PMMA and PSAF-assisted transfer processes. (a) A wet-transfer process using PMMA supporting layer. The morphology of the PMMA layers is rigid and reverse to the rough surface of Cu. The unmatched morphologies between PMMA and target surfaces (incomplete wetting) result in occurrence of ripples and tears during the dissolution of PMMA. (b) A dry transfer using PSAF includes the complete wetting step, where the liquid-like PSA layer adapts its morphology to target surface as soft pressure applied on it.

Figure 3-2 shows a comparison between PMMA and PSAF-assisted transfer methods. The morphology of the PMMA layers is rigid and reverse-templated by the rough-textured Cu surface (Figure 3-2a). Therefore, the surface morphologies of PMMA and target substrates do not match, leading to

incomplete wetting at the interface and the formation of ripples and tears after dissolving the PMMA. On the other hand, dry transfer using PSAF enables complete wetting of graphene on the target surface, as the liquid-like PSA layer adapts its morphology to the surface (Figure 3-2b). As a result, the van der Waals contact area between graphene and the target substrate could be maximized, and the formation of ripples and cracks can be minimized during the peel-off process. In addition, we suppose that graphene tends to be more easily transferred to SiO_2 or glass substrates because of the stronger charge-transfer interaction between graphene and oxygen-rich surface. [22,23]

Table 3-1. Surface energy and contact angle of substrates and graphene transferred on each substrate. The surface energy is calculated from contact angle measurement of water and di-iodomethane based on Owen-Wendt model.

	SiO_2/Si	G/SiO_2/Si	PSAF	G/PSAF
γ (dyn/cm)	94.21	32.59	14.16	22.15
γ^d (dyn/cm)	3.83	0.51	13.38	19.21
γ^p (dyn/cm)	90.38	32.08	0.78	2.94
θ (°)	21.26	80.26	109.67	93.36
Optical image	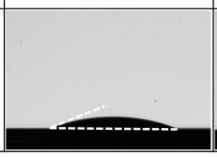	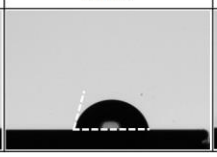	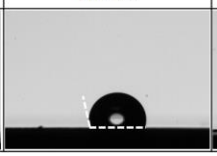	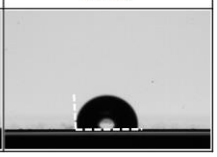

To compare the surface energies of various substrates with or without graphene, we measured the contact angles of water droplets on SiO_2/Si, PSAF, graphene on SiO_2/Si, and graphene on PSAF. As shown in Table S1, the SiO_2/Si surface shows the smallest contact angle, i.e., the largest surface energy. Therefore, the weakly bound graphene on PSAF can be transferred to

SiO_2/Si substrates due to the large difference in their surface energies (94.21 dyn/cm vs. 14.16 dyn/cm). [9]

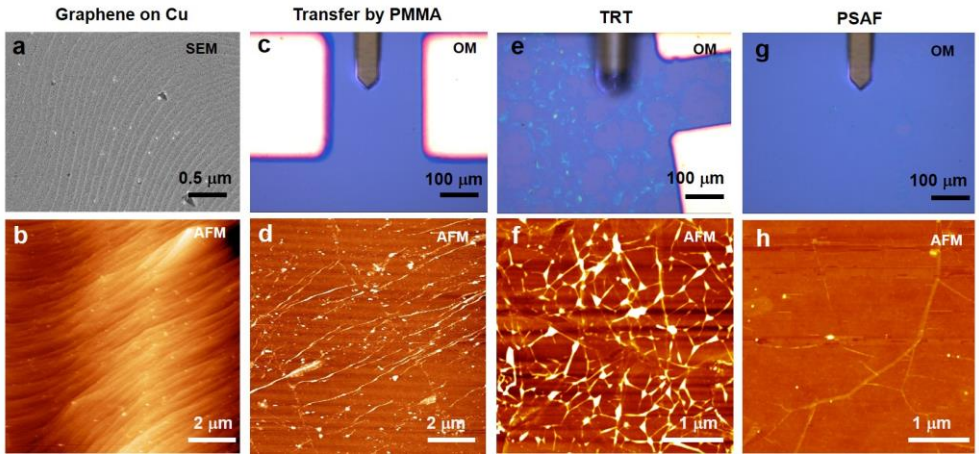

Figure 3-3. Comparison between PMMA, TRT and PSAF-transferred graphene. (a, b) SEM and AFM images of as-grown graphene on Cu, showing periodic steps of Cu. (c, d) OM and AFM images of PMMA-transferred graphene on SiO_2, showing PMMA residues and ripples reversely templated by Cu steps. (e, f) OM and AFM images of TRT-transferred graphene on SiO_2. The large thermal deformation of the release and target films at the temperature close to their T_g (glass transition temperature) resulted in the occurrence of ripples on polymer residues. (g, h) OM and AFM images of PSAF-transferred graphene on SiO_2, showing ultraclean surface without residues and periodic ripples. The thick ripples originate from the negative thermal expansion of graphene.

The cleanness and flatness of graphene surface transferred by different supporting polymers were investigated by scanning electron microscopy (SEM), optical microscopy (OM), and AFM, with representative images shown in Figure 2. The surface of as-grown graphene on Cu often shows periodic steps formed by recrytallization (Figure 3-3a,b). [24-25] Therefore, the spin-coated PMMA surface, which is reverse templated with respect to the

periodic textures on Cu, does not match well with the flatness of target substrates. As a result, graphene transferred onto flat SiO_2 can undergo incomplete wetting, leading to formation of ripples or cracks (Figure 3-3c,d). This problem is more serious for the TRT-transferred graphene because it needs to be heated up to 100-120 ℃ in order to release graphene films, and the large thermal deformation of polymer films tends to result in the occurrence of ripples on polymer residues (Figure. 3-3e,f). On the other hand, the PSAF-transferred graphene shows an ultraclean surface almost without residues and periodic ripples (Figure. 3-3g,h)..

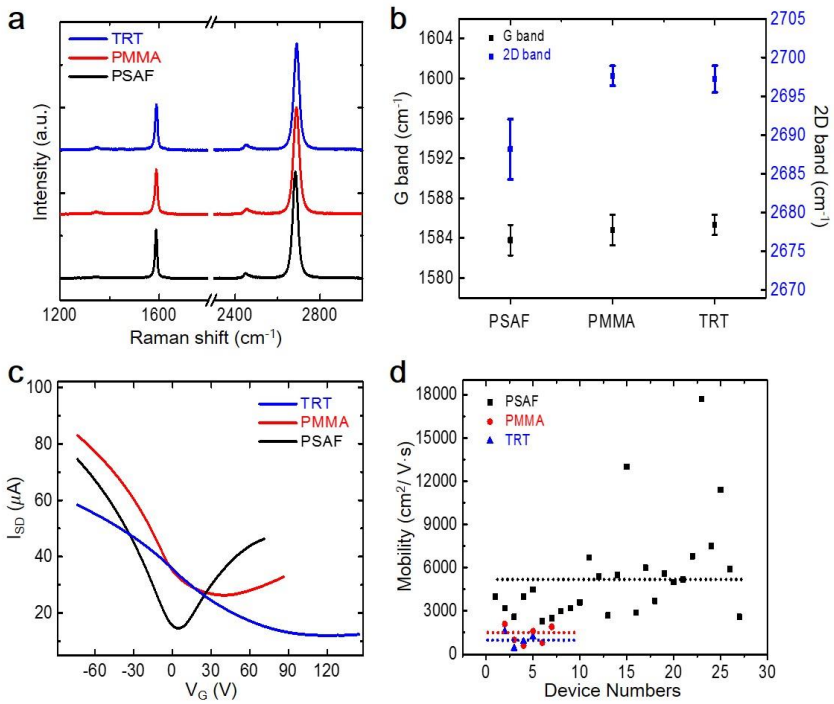

Figure 3-4. Characteristics of PSAF-transferred graphene compared with TRT and PMMA- transferred graphene. (a) Raman spectra of graphene films transferred on SiO_2/Si substrates (excitation wavenumber, 514nm). (b) G and 2D band shift of graphene, indicating that the PSAF-transferred graphene is much less p-doped. (c) FET characteristics of graphene films on SiO_2/Si substrates (V_{sd}= 10 mV). (d) Mobility distribution of graphene FET devices. Average carrier mobility of PSAF, PMMA and TRT-transferred graphene are ~5,300 $cm^2/V \cdot s$, ~1,500 $cm^2/V \cdot s$, and ~1,000 $cm^2/V \cdot s$, respectively.

Figure 3-4a shows Raman spectra of graphene transferred onto Si/SiO_2 substrates using the three polymer films. The negligible D peak intensities and the large 2D/G peak ratio indicate that the as-synthesized CVD graphene is a high-quality single layer. The G and 2D band peaks of graphene samples transferred using PMMA and TRT films are blue-shifted compared to those transferred using PSAF (Figure 3-4b), implying that the

PSAF-transferred graphene is almost free from polymer residues that give rise to *p*-doping. [26] In addition, X-ray photoelectron spectroscopy (XPS) analysis of graphene transferred by PSAF clearly shows the narrower spectral width of the C1s peak than the case of using TRT, indicating the cleanness of the graphene surface (Supporting Information, Figure 3-5). This observation is in good agreement with the FET measurement results showing the Dirac voltage at V_{Dirac}= ~3 V for PSAF-transferred graphene, which is in contrast to those of PMMA and TRT-transferred graphene at V_{Dirac}= ~40 V and ~113 V, respectively (Figure 3-4c). This ultraclean and undoped graphene surface is expected to be advantageous for better electrical properties. Indeed, the field-effect mobility of PSAF-transferred graphene on SiO_2/Si is as high as 17,700 cm^2 /V·s, which is a few times higher than that of PMMA-transferred graphene (Figure 3-4d). The average carrier mobilities of PSAF, PMMA and TRT-transferred graphene are ~5,300 cm^2/V•s, ~1,500 cm^2/V•s, and ~1,000 cm^2/V•s, respectively.

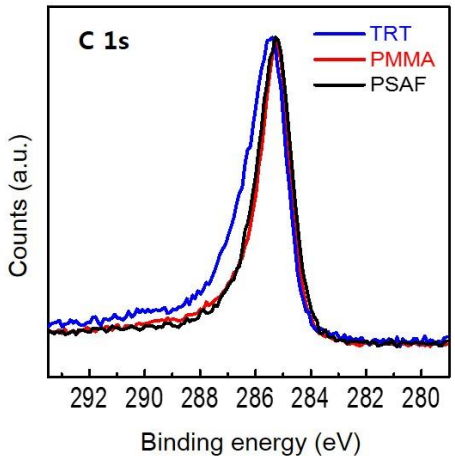

Figure 3-5. XPS spectra of graphene transferred by PSAFs, PMMA and TRT film, respectively. XPS analyses were carried out using Thermo Scientific K-Alpha (small-spot X-ray Photoelectron Spectrometer system)

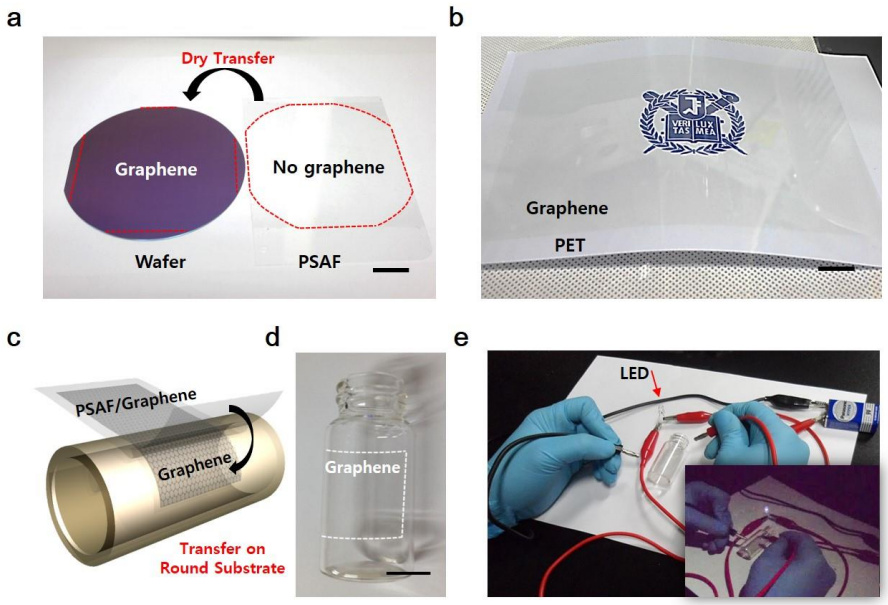

Figure 3-6. PSAF-assisted transfer of large-area graphene films on various substrates. (a-d) Graphene on a 4-inch wafer, a B5-sized PET film, and a round substrate, respectively. Scale bar, 2 cm. (e) Demonstration of a light-emitting diode (LED) connected through the graphene sheet, indicating that the transferred graphene is continuous. Operating voltage, 9V.

Photographs of the transferred graphene on a 4-inch SiO_2/Si wafer and a PET film (Figure 3-6a, b) show that the PSAF-assisted transfer method is applicable to both rigid and flexible substrates without difficulty in scaling up. We also confirmed that the graphene on the PSAF can be easily transferred on arbitrarily shaped substrates at room temperature (Figure 3-6c, d). A light-emitting diode (LED) connected through the graphene sheet transferred by PSAF was turned on at 9V, indicating that the graphene is electrically continuous on the curved surface (Figure 3-6e).

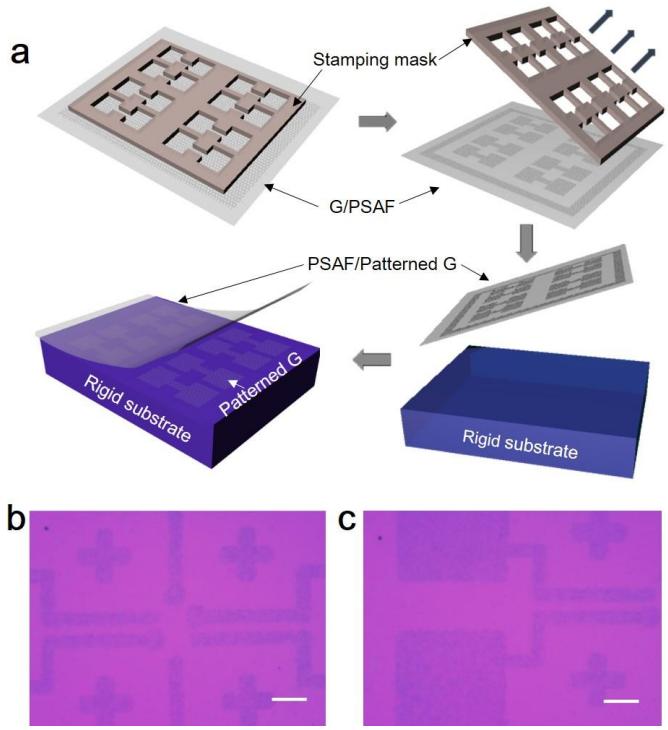

Figure 3-7. Patterned transfer of large-area graphene using PSAF and stamping masks. (a) A schematic representation showing the patterning and transfer steps. (b-c) Graphene electrodes patterned on a SiO_2/Si substrate using PSAF and the stamping mask. Scale bars, 100 μm.

Figure 3-7a shows a schematic of patterning and transferring graphene utilizing PSAF without relying on conventional lithography steps that include photoresist or e-beam resist coating and removal. First, a stamping mask with a minimum pattern width of ~50μm is brought into soft contact (~ 1.0 Mpa) with graphene on PSAF. The stamping mask is then removed, carrying with it the contacted graphene due to stronger adhesion, and leaving behind the inverse pattern on the PSAF. Finally, the PSAF is put on a rigid substrate with the graphene side down, and the remaining graphene area is fully transferred to the substrate. It should be noted that this patterning method does not include any wet treatment that might cause unexpected contamination on graphene surface.

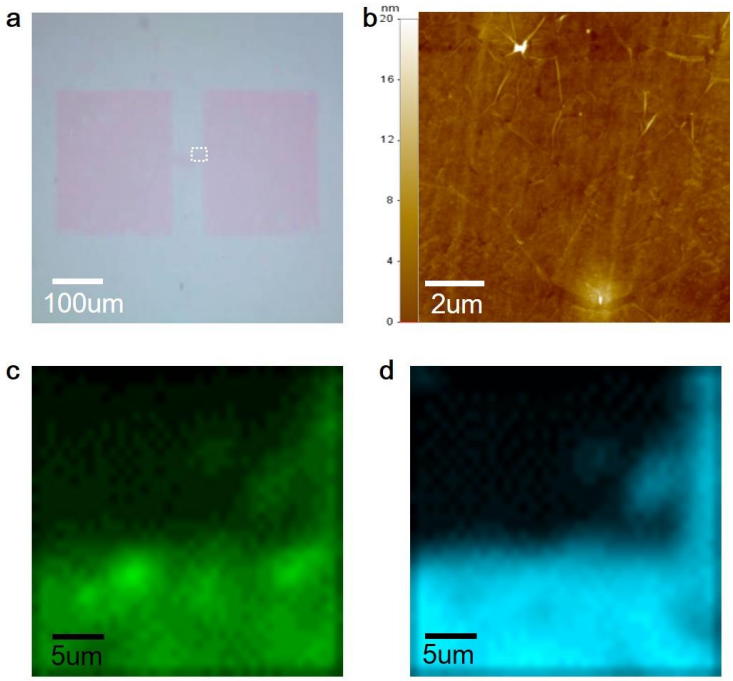

Figure 3-8. Optical, AFM and Raman analyses of the PSAF-patterned graphene. (**a**) An optical image of patterned graphene on a SiO_2/Si substrate. (**b**) An AFM image (10μm×10μm) of transferred graphene on Polyimide (PI) film by roll-to-roll process. (**c-d**)Two-dimensional Raman mapping of G and 2D peaks, respectively, corresoponding to the dashed white box in a.

The OM images show that the graphene has been well patterned by using the PSAF and the stamping mask as shown in Figure 3-7b,c and Figure 3-8a. We also confirmed that only a negligible amount of residue remained on the surface of graphene when transferred on a polyimide (PI) substrate by a roll-to-roll transfer process (Figure 3-8b). Finally, the recyclability of PSAFs was evaluated by measuring the changes in sheet resistance and optical transmittance with respect to the number of reuses, which is important for more cost-effective production of graphene films.

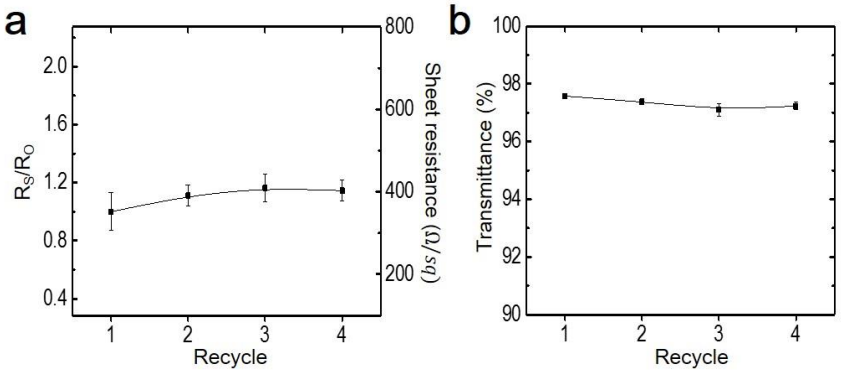

Figure 3-9. Change in the optoelectronic properties of single layer graphene with respect to the number of PSAF recycling. (a) Sheet resistance change of graphene transferred by recycled PSAF. (b) Transmittance change of graphene transferred by recycled PSAF.

Figure 3-9 shows that the electrical and optical properties of graphene transferred by recycled PSAFs did not change significantly up to 4 times, which is contrasted with TRT or PMMA films that are not recyclable. In addition, we confirmed the excellent uniformity of the graphene film transferred by PSAF on a PET film by mapping the sheet resistance of a large-are sample (80×120 mm^2) (Figure 3-10). [27]

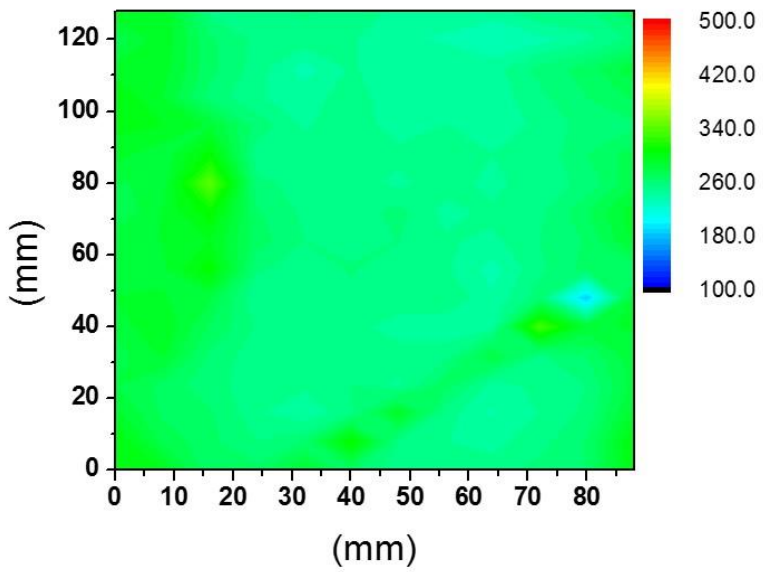

Figure 3-10. Sheet resistance mapping that shows the large-area uniformity of the graphene film transferred by PASF. The transfer process was carried out by a roll-to-roll transfer method. The ammonium persulfate (APS) and benzimidazole (BI) mixed in an acidic solution were was used as p-doping Cu etchant. Color scale, Ohm/sq. The average sheet resistance is ~250 Ohm/sq.

In conclusion, we have demonstrated the ultra-clean patterned-transfer of single-layer graphene by recyclable pressure sensitive adhesive films at room temperature. This simple transfer was enabled by controlling the adhesion energy difference between PSAF and target substrates. The resulting PSAF-transferred graphene shows much less *p*-doping and electron mobility as high as 17,700 $cm^2/V \cdot sec$, implying that the graphene surface is ultraclean and free from mechanical damages. In addition, the sheet resistance of graphene transferred by recycled PSAF does not change considerably up to 4 times, which would be advantageous for more cost-effective and environmentally friendly production of large-area graphene films.

3.4. Methods

PSAF preparation. Pressure sensitive adhesive (PSA) consisted with a mixture of silicone based adhesive solutions (Dow corning). The PSAs were made by a mixture of DOW CORNING® 7646 ADHESIVE : DOW CORNING® 7652 ADHESIVE : toluene with a mass ratio of 7: 3: 10. After stirred for 5 hours, additionally, SYL-OFF® SL 7028 CROSSLINKER and SYL-OFF® SL 9250 ANCHORAGE ADDITIVE were added in the mixture (mass ratio of 1 : 200), respectively. Additionally, SYL-OFF® 4000 CATALYST added in total mixture and stirred 1hour. Finally, PSA solution were spin-coated on the PET substrates (4000 rpm, 30sec) and basked at 150 ^{o}C for 1 min.

PSAF transfer. The PSAF was coated on the graphene film and Cu catalyst was etched by 0.1M ammonium persulfate (APS) solution. After completely removing Cu by further etching, the graphene on the PSAF was rinsed with DI water and stored in dehydrated condition (30min) for dry transfer. The graphene on the PSAF was attached to the target substrates by week pressing or rolling methods with normal stress of 4 N/mm^{2}.[6] The speed and the angle of peeling-off with respect to substrate surface were 2 mm/sec and ~90^{o}, respectively.

Characterization. The AFM image was measured by a noncontact mode (Park System, XE-100). XPS analyses were carried out using Thermo Scientific K-Alpha (small-spot X-ray Photoelectron Spectrometer system).

The Raman spectra were measured by a Raman spectrometer (RM 1000-Invia, Renishaw, 514nm). The optical transmittance of graphene was measured using an ultraviolet-visible spectrometer (UV-3600, Shimazdu). The sheet resistance was measured with 4-point probe nanovoltmeter (Keithley 6221), and the current-voltage curve was measured by Agilent B2912A.

3.5. References

1. Kang, J.; Shin, D.; Bae, S.; Hong, B.H. *Nanoscale* **2012**, *4*, 5527-5537.

2. Li, X.; Zhu, Y.; Cai, W.; Borysiak, M.; Han, B.; Chen, D.; Piner, R. D.; Colombo, L.; Ruoff, R. S. *Nano Lett.* **2009**, *9*, 4359-4363.

3. Li, X.; Cai, W.; An, J.; Kim, S.; Nah, J.; Yang, D.; Piner, R.; Velamakanni, A.; Jung, I.; Tutuc, E.; Banerjee, S. K.; Colombo, L.; Ruoff, R. S. *Science* **2009**, *324*, 1312-1314.

4. Gao, L.; Ren, W.; Xu, H.; Jin, L.; Wang, Z.; Ma, T.; Ma, L.-P.; Zhang, Z.; Fu, Q.; Peng, L.-M.; Bao, X.; Cheng, H.-M. *Nat Commun.* **2012**, *3*, (699), 1-7.

5. Bae, S.; Kim, H.; Lee, Y.; Xu, X.; Park, J.-S.; Zheng, Y.; Balakrishnan, J.; Lei, T.; Kim, H.R.; Song, Y. I.; Kim, Y.-J.; Kim, K. S.; Ozyilmaz, B.; Ahn, J.-H.; Hong, B. H.; Iijima, S. *Nat Nanotechnol.* **2010**, *5*, 574-578.

6. Kang, J.; Hwang, S.; Kim, J. H.; Kim, M. H.; Ryu, J.; Seo, S. J.; Hong, B. H.; Kim, M. K.; Choi, J.-B. *ACS Nano* **2012**, *6*, 5360-5365.

7. Lee, Y.; Bae, S.; Jang, H.; Jang, S.; Zhu, S.-E.; Sim, S. H.; Song, Y. I.; Hong, B. H.; Ahn, J.-H. *Nano Lett.* **2010**, *1*, 490-493.

8. Liang, X.; Fu, Z.; Chou, S. Y. *Nano Lett.* **2007**, *7*, 3840-3844.

9. Kang, S. J.; Kim, B.; Kim, K. S.; Zhao, Y.; Chen, Z.; Lee, G. H.; Hone, J.; Kim, P.; Nuckolls, C. *Adv. Mater.* **2011**, *23*, 3531-3535.

10. Chen, X.-D.; Liu, Z.-B.; Zheng, C.-Y.; Xing, F.; Yan, X.-Q.; Chen, Y.; Tian, J.-G. C*arbon* **2013**, *56*, 271-278.

11. Regan, W.; Alem, N.; Alemán, B.; Geng, B.; Girit, Ç.; Maserati, L.; Wang, F.; Crommie, M.; Zettl, A. *Appl. Phys. Lett.* **2010**, *96*, 113102.

12. Yoon, T.; Shin, W. C.; Kim, T. Y.; Mun, J. H.; Kim, T.-S.; Cho, B. J. *Nano Lett.* **2012**, *11*, 1448-1452.

13. Lin, Y.-C.; Jin, C.; Lee, J.-C.; Jen, S.-F.; Suenaga, K.; Chiu, P.-W. *ACS Nano* **2011**, *5*, 2362-2368.

14. Cheng, Z.; Zhou, Q.; Wang, C.; Li, Q.; Wang, C.; Fang, Y. *Nano Lett.* **2011**, *11*, 767-771.

15. Kim, K. S.; Zhao, Y.; Jang, H.; Lee, S. Y.; Kim, J. M.; Kim, K. S.; Ahn, J.-H.; Kim, P.; Choi, J.-Y.; Hong, B. H. *Nature* **2009**, *457*, 706-710.

16. Levendorf, M. P.; Ruiz-Vargas, C. S.; Garg, S.; Park, J. *Nano Lett.* **2009**, *9*, 4479-4483.

17. Bai, J.; Zhong, X.; Jiang, S.; Huang, Y.; Duan, X. *Nat Nanotechnol.* **2010**, *5*, 190-194.

18. Dimiev, A.; Kosynkin, D. V.; Sinitskii, A.; Slesarev, A.; Sun, Z.; Tour, J. M. *Science* **2011**, *331*, 1168-1172.

19. Sinitskii, A.; Tour, J. M. *J. Am. Chem. Soc.* **2010**, *132*, 14730-14732.

20. Zhang, L.; Diao, S.; Nie, Y.; Yan, K.; Liu, N.; Dai, B.; Xie, Q.; Reina, A.; Kong, J.; Liu, Z. *J. Am. Chem. Soc.* **2011**, *133*, 2706-2713.

21. Safron, N. S.; Kim, M.; Gopalan, P.; Arnold, M. S. *Adv. Mater.* **2012**, *24*, 1041-1045.

22. Fan, X. F.; Zheng, W. T.; Chihaia, V.; Shen, Z. X.; Kuo, J.-L. *J. Phys.: Condens. Matter* **2012**, *24*, 305004.

23. Rudenko, A. N.; Keil, F. J.; Katsnelson, M. I.; Lichtenstein, A. I. *Phys. Rev. B.* **2011,** *84*, 085438.

24. Ni, G.-X.; Zheng, Y.; Bae, S.; Kim, H. R.; Pachoud, A.; Kim, Y. S.; Tan, C.-L.; Im, D.; Ahn, J.-H.; Hong, B. H.; Ö zyilmaz, B. *ACS Nano* **2012**, 6, 1158-1164.

25. Kim, D. W.; Lee, J.; Kim, S. J.; Jeon, S.; Jung, H.-T. *J. Mater. Chem. C* **2013**, 1, 7819-7824.

26. Ferrari, A. C.; Meyer, J. C.; Scardaci, V.; Casiraghi, C.; Lazzeri, M.; Mauri, F.; Piscanec, S.; Jiang, D.; Novoselov, K. S.; Roth, S.; Geim, A. K. *Phys. Rev. Lett.* **2006**, *97*, 187401.

27. Kim, S. J.; Ryu, J.; Son, S.; Yoo, J. M.; Park, J. B.; Won, D.; Lee, E.-K.; Cho, S.-P.; Bae, S.; Cho, S.; Hong, B. H. *Chem. Mater*. **2014**, *26*, 2332-2336.

Chapter 4. Optimization by Surface Functionalization.

- Surface-Engineered Graphene Quantum Dots Incorporated into Polymer Layers for High Performance Organic Photovoltaics †

† This is reproduced from Jung Kyu Kim,* Sang Jin Kim,* Myung Jin Park, Sukang Bae, Sung-Pyo Cho, Qing Guo Du, Dong Hwan Wang, Jong Hyeok Park, and Byung Hee Hong, *Sci. Rep.* **2015**. © 2015, Nature Publishing Group. (accepted)

4.1. **Abstract**

Graphene quantum dots (GQDs), a newly emerging 0-dimensional graphene based material, have been widely exploited in optoelectronic devices due to their tunable optical and electronic properties depending on their functional groups. Moreover, the dispersibility of GQDs in common solvents depending on hydrophobicity or hydrophilicity can be controlled by chemical functionalization, which is particularly important for homogeneous incorporation into various polymer layers. Here we report that a surface-engineered GQD-incorporated polymer photovoltaic device shows enhanced power conversion efficiency (PCE), where the oxygen-related functionalization of GQDs enabled good dispersity in a PEDOT:PSS hole extraction layer, leading to significantly improved short circuit current density (Jsc) value. To maximize the PCE of the device, hydrophobic GQDs that are hydrothermally reduced (rGQD) were additionally incorporated in a bulk-heterojunction layer, which is found to promote a synergistic effect with the GQD-incorporated hole extraction layer.

4.2. Introduction

Donor-acceptor blended bulk heterojunction (BHJ) organic photovoltaic devices (OPVs) are considered promising next generation solar cells due to their low-cost, light weight, flexibility, and solution processability[1-3]. However, because the thickness of BHJ layer was restricted, the insufficient carrier mobility of the BHJ have limited its light absorption capability[4,5]. Therefore, numerous researches have endeavored to enhance the power conversion efficiency (PCE) of the devices by incorporating methods such as introducing newly designed and synthesized donor or acceptor molecules, embedding metal nanoparticles into organic layers, modifying the bimolecular morphology, or introducing interlayer engineering to the electron or hole extraction layer[6-11]. Especially the light absorption and charge transport performances were considerably ameliorated by incorporating shape-controlled Ag or Au nanomaterials such as nanoparticles or nanorods into the polymer layers in OPVs[12-14]. It is because the OPVs can utilize the incident light scattering and surface plasmon (SPR) effects of the metal nanometarials. Furthermore, the high electric conductance of the embedded metal nanomaterials increase the charge transport performance within the polymer layers[13-18]. However, the metal nanomaterials might inflict damage or a short circuit problem on the devices owing to the undesired morphological distortions in the embedded layers or aggregation of the nanomaterials[49,50]. Furthermore, metal nanomaterials have lots of potential to induce monomolecular recombination, acting as trap sites and resulting in an

inefficient hole extraction from the BHJ layers[19,50]. Recently, insulator coated nanostructures such as SiO_2 coated Au or Ag nanoparticles have also been embedded in the BHJ or poly(3,4-ethylenedioxythiophene):poly(4-styrenesulfonate) (PEODT:PSS) layers[20-21]. Although this process can alleviate the risk of short circuit and improve the PCE, the particle size is out of proportion to the OPVs, because it is difficult to say the 80 nm particles are deeply embedded in the 80 nm thick BHJ layer or 40 nm thick PEDOT:PSS layer[50]. In addition, it is difficult to tune the optoelectronic properties of the nanoparticles owing to the control problem of their size or shape.

Recently, our group introduced the graphene quantum dots (GQDs) in the BHJ layer of OPVs[22]. GQDs have been considered as an emerging material for optoelectronic applications, due to their tunable band gap, low toxicity, environmental compatibility and chemical inertness[22-33]. The optical and electrical properties of GQDs were readily tuned by controlling their chemical functionalities. Noticeable enhancement of PCE was recorded by incorporating reduced GQDs (rGQD) into BHJ layer only in very small quantities. Moreover, the possibility of the short circuit was evitable within the GQD-embedded polymer layers because GQDs exhibit non-metallic behaviors with sufficient band gap energy unlike the conventional metal nanomaterials[22].

In this study, to maximize the dispersion stability of GQDs in PEDOT:PSS (AI4083), we synthesized GQDs with sufficient oxygen based functionalities by using a simple process based on the acidic treatment of carbon fibers[34]. The GQDs were well dispersed in the polar solvent and

PEODT:PSS without any severe aggregations due to the oxygen-related functionalities on the surface of GQDs. In order to investigate their positive effects in OPVs, the BHJ layer composed of thieno[3,4-b]-thiophene/ benzodithiophene (PTB7) and [6,6]-phenyl C_{71} butyric acid methyl-ester ($PC_{71}BM$) was spin coated on top of the GQDs incorporated PEDOT:PSS layer. The fabricated devices with GQDs showed high efficient polymer based BHJ solar cells without risking the irrecoverable damages. Furthermore, the additionally incorporated rGQD in the BHJ layer were found to promote a synergistic effect with the GQD-incorporated hole extraction layer.

4.3. Results and discussions

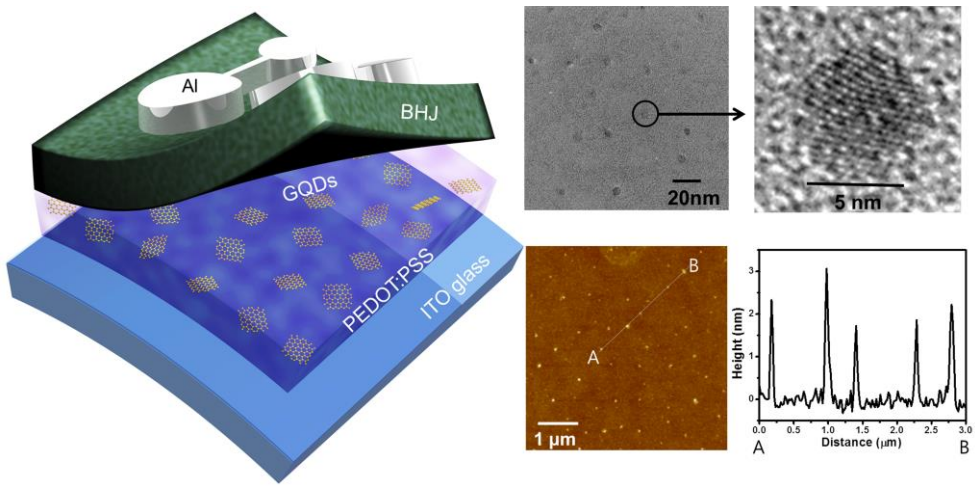

Figure 4-1. Schematic of device, and TEM and AFM images of GQDs. Schematic of OPV device with a GQD-incorporated PEDOT:PSS layer, and TEM images of the GQDs. The scale bar is 20nm on the TEM image, and 5nm on the inset image. AFM image of GQDs (5 μm by 5 μm) and height distribution from A to B.

Fig. 4-1 displays transmission electron microscope (TEM) and atomic force microscope (AFM) images of as-synthesized GQDs with uniform diameter of ~ 5nm. The height of GQDs were ~2 nm, which reflect the number of layers in GQDs was approximately 3-4 layers, as evident from the AFM line profile. Fourier Transform Infrared Spectroscopy (FT-IR) and X-ray Photoelectron Spectroscopy (XPS) measurements were carried out to determine the composition of GQDs. Fig. 4-2A shows FT-IR spectrum of GQDs in the range of 4000~400 cm^{-1}, and exhibits the characteristic absorption bands corresponding to the stretching and bending vibration of -OH groups at 3452 cm^{-1}, C=C stretching at 1637 cm^{-1}, O-H deformation vibration at 1384 cm^{-1}, phenolic hydroxyl group stretching of C-OH groups at

1265 cm^{-1}, C-O vibration groups at 1095 cm^{-1}, and epoxy stretching vibration of C-O-C groups at 1049 cm^{-1}. In the C1s XPS spectrum of GQDs in Fig. 4-2B, three different peaks were decomposed, centered at 284.7, 286.4 and 288.2 eV, corresponding to sp^2 carbon aromatic rings (C=C), C-O and C=O, respectively. The distinguished C-O and C=O peaks imply that the oxygen-related functional groups such as hydroxyl and carboxyl groups are on the edges of GQDs. Therefore, the functionalities could contribute to the dispersion of GQDs in polar solvents. In order to incorporate the GQDs into the PEODT:PSS solution, as-synthesized GQDs were blended in methanol, and were mixed with the PEDOT:PSS solution. The methanol does not have significantly negative effects on device performances, because it has been widely used as an additive or co-solvent for the PEDOT:PSS layer to improve the film morphology[35].

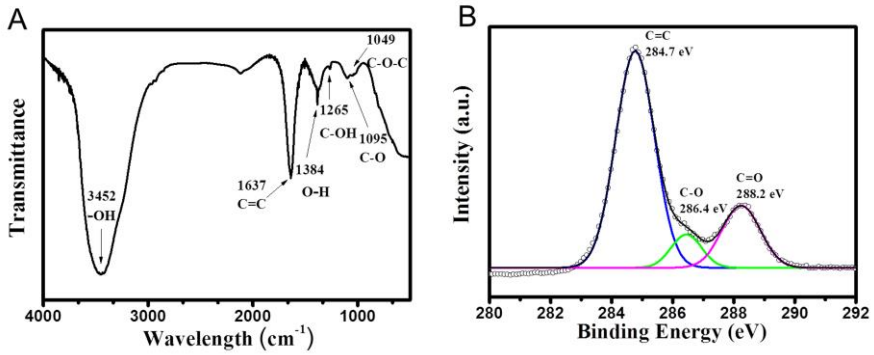

Figure 4-2. Characteristics of GQDs. FT-IR (A) and XPS C1s (B) spectra of GQDs.

4.3.1. Surface morphologies of the GQDs-incorporated PEDOT:PSS film.

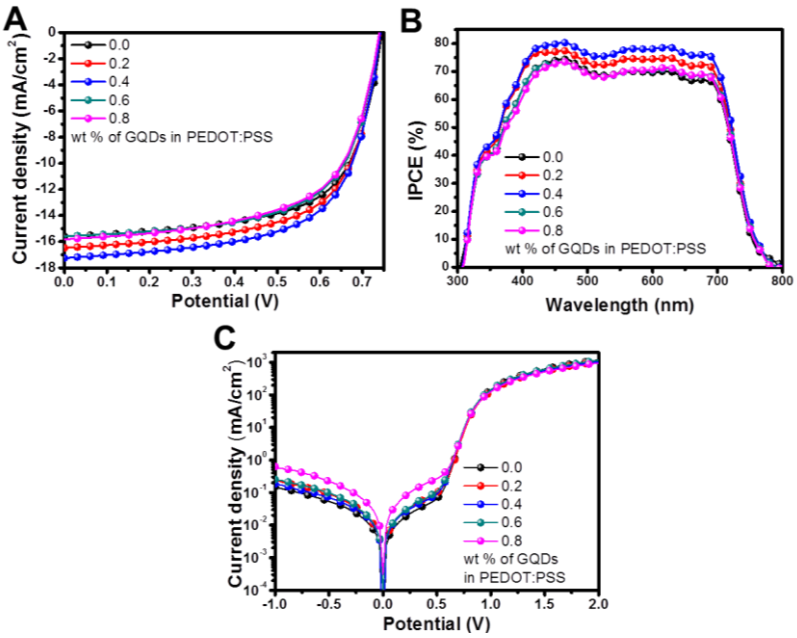

Figure 5-3. Current vs. potential (J-V) curves (A), incident photon-to-charge-carrier-efficiency (IPCE) (B) and dark current density-potential curves (C) of the devices with various GQD concentrations in the PEDOT:PSS layer. The performance parameters of the devices were exhibited in **Table 4-1**.

Table 4-1. Performance parameters of OPVs with various concentrations of GQDs incorporated into the PEDOT:PSS layer.

GQD (wt %)	V_{oc} (V)	J_{sc}(mA/cm^2)	FF(%)	*PCE(%)	R_{sh}(KΩcm^2)
0.0	0.746 (±0.001)	15.6 (±0.01)	64.8 (±0.13)	7.52 (±0.08)	12.20
0.2	0.740 (±0.001)	16.5 (±0.13)	63.9 (±0.04)	7.81 (±0.07)	8.20
0.4	0.741 (±0.001)	17.3 (±0.03)	64.0 (±0.16)	8.17 (±0.08)	8.57
0.6	0.742 (±0.002)	15.6 (±0.02)	63.6 (±0.23)	7.35 (±0.11)	7.74
0.8	0.740 (±0.001)	15.8 (±0.02)	61.8 (±0.19)	7.22 (±0.08)	3.09

GQD-incorporated PEDOT:PSS layers were prepared by incorporating the GQDs/methanol solution in the PEDOT:PSS solution with varying weight ratio from 0.2 to 0.8 wt. %. Optimum device efficiency of 8.17 % was accomplished by incorporating 0.4 wt. % of GQDs into the PEDOT:PSS layer as shown in Fig. 4-3. Though significantly lower quantity of GQDs were used in this study comparing to those of other metal nanomaterials in previous reports, GQDs comparably improved the device performance[12-18,20,21].

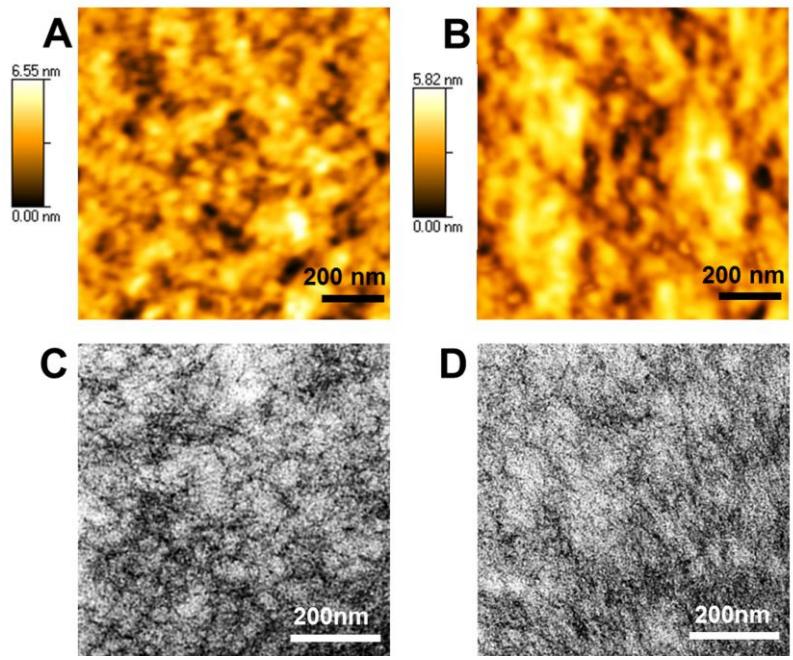

Figure 4-4. AFM and TEM images of PEDOT:PSS film. AFM images of PEDOT:PSS films without GQDs (A) and incorporating GQDs (B), which were spin coated on top of the ITO glass. Spherical aberration corrected transmission electron microscopy (Cs-corrected TEM) images of PEDOT:PSS film without (C) and with (D) GQDs. GQD concentration was 0.4 wt %.

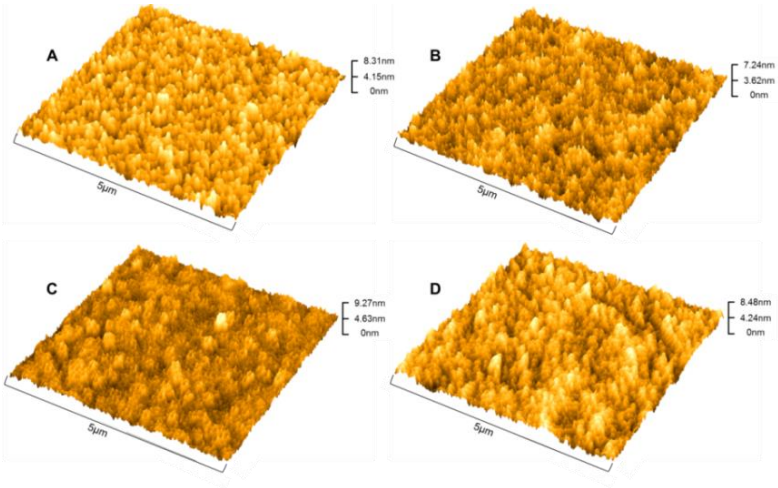

Figure 4-5. (A) AFM images of the PEDOT:PSS layer without GQDs, and with various ratios of GQDs: (B) 0.2, (C) 0.4 and (D) 0.6.

Fig. 4-4 and 4-5 show the AFM images of GQDs incorporated into PEDOT:PSS films. GQDs were well dispersed in the PEDOT:PSS layer without any significant cracks, due to the high dispersion of GQDs in polar solvents. After the GQDs-incorporated PEDOT:PSS film was formed on the ITO substrate via spin-coating, OPV devices were fabricated following the conventional procedures. Fig. 4-4A and B show AFM topography images of the PEDOT:PSS films w/o and w/ GQDs, respectively. In a bare PEDOT:PSS, because it is difficult to form a uniform PEDOT layer on a substrate, the negatively charged PSS is doped in the positively charged PEDOT to enhance the dispersion property in polar solvent. The insulating PSS domains surround the highly conducting PEDOT domains, thereby the grain of PEDOT:PSS is composed of PEDOT-rich core and PSS-rich shell[36-40]. In addition, the grain size of PEDOT:PSS is usually determined by hydrogen bonds between PSS-

rich shells[51]. Fig. 4-4B indicates that the grain size of GQDs-incorporated PEDOT:PSS film is outstandingly increased while the grain boundaries are spread out more evenly. The GQDs with sufficient oxygen based functionalities intervene in the domain formation between PEDOT and PSS to determine the morphology of PEDOT:PSS film.

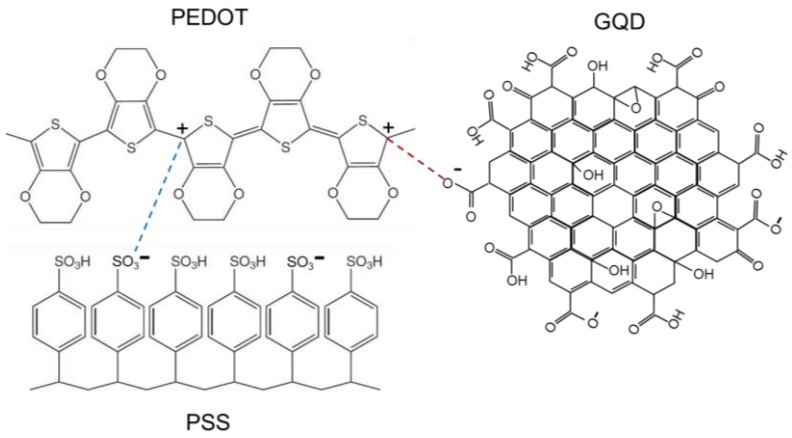

Figure 4-6. Schematic of chemical structures of PEDOT, PSS and GQD.

The negatively charged GQDs can increase the size of PEDOT-rich cores because the positively charged PEDOT polymers combine with GQDs (Fig 4-6.). Thereby, the decreased net charge of PEDOT results in lowering the electrostatic interaction between PEDOT-rich and PSS-rich domains. In addition, we obtained Cs-corrected TEM images as shown in Fig. 4-4C and 4-4D in order to understand the positive effects of GQDs in terms of the morphology properties. Unfortunately, it was difficult to visualize their domain structures from the Cs-corrected TEM images because all the components in the PEDOT:PSS layer has similar atoms. However, we

observed that the skein-like black wires, which presumably indicated grain boundaries, were untangled in Fig. 4-4D when compared with Fig. 4-4C (without GQDs). This results indicate that grain size of PEDOT:PSS film was increased because of the interaction between PEDOT and the incorporated GQDs. The grain size of both PEDOT:PSS films with or without GQDs were quantified using a line measurement with AFM images in Fig 4-7.

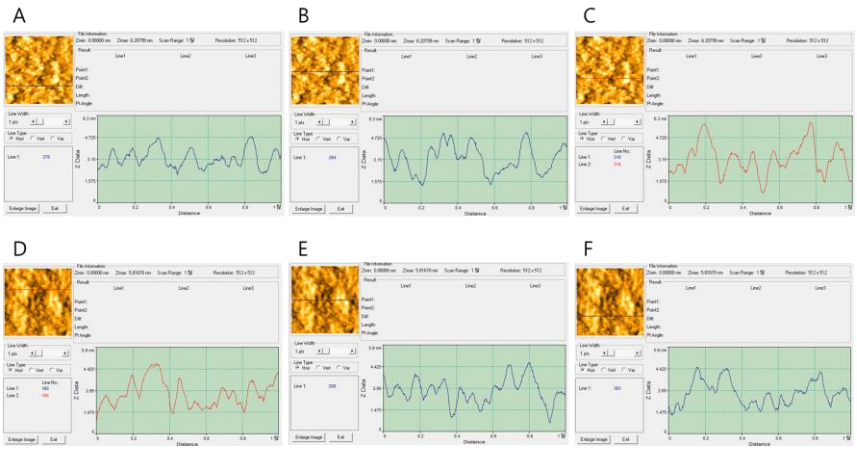

Figure 4-7. Line measurement results of the surface morphology of the bare PEDOT:PSS film (A)~(C), and the GQD-incorporated PEDOT:PSS film (D)~(F). The average values of the estimated grain size were around 30 nm for the bare PEDOT:PSS, and around 70 nm for the GQD-incorporated PEDOT:PSS. The line measurement was conducted using SPM Lab Analysis software (Veeco instruments, Inc.)

4.3.2. Photovoltaic performance of the OPVs.

The GQDs-incorporated device exhibits considerably improved PCE. Here, the PCE was determined by the intensity of power that a device generates using a given power of solar light at the maximum power.

$$\text{PCE} = \frac{Maximum\ power\ from\ our\ cell\ (J_{sc} \times FF \times V_{oc})}{Power\ of\ solar\ light\ (100\ ^{mW}/_{cm^2})} \quad (1)$$

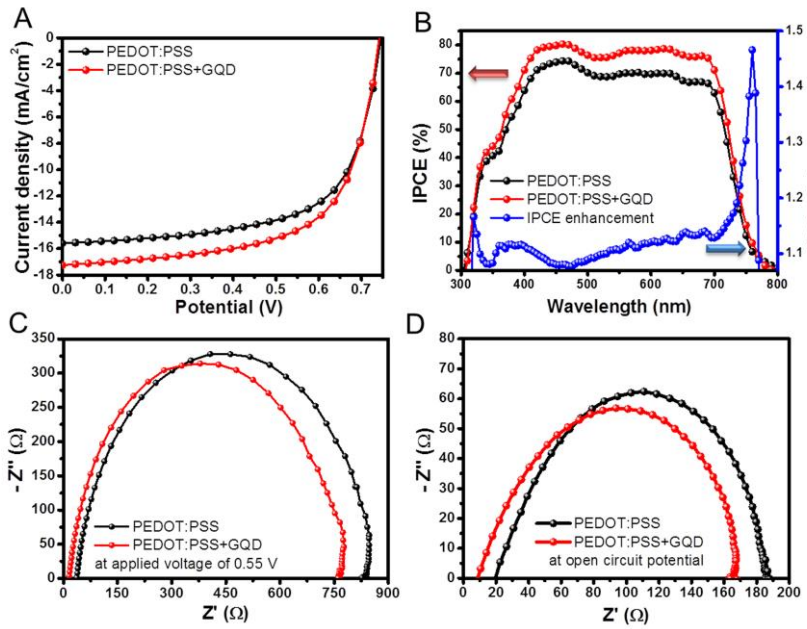

Figure 4-8. Device performance and characterization. Current vs. potential (J-V) curves (A), and incident photon-to-charge-carrier-efficiency (IPCE) and IPCE enhancement factor for the devices (B). Nyquist plots of electrochemical impedance spectroscopy at 0.55 V (C) and at open circuit potential (D). 0.4 wt. % of GQDs was incorporated into PEDOT:PSS layer.

Among the parameters in this study, J_{sc} was significantly improved from 15.6 mA/cm^2 to 17.3 mA/cm^2 as shown in Fig. 4-8A and 4-8B, and Table 4-2. We confirmed that the enhanced J_{sc} was dominantly contributed to the improvement of PCE of the GQDs-incorporated PEDOT:PSS device (GQDs in HTL) through the incident photon to current conversion efficiency (IPCE) measurement. IPCE is defined by the number of injected electrons from the excited cites under the monochromatic light divided by pre-defined input photon flux. Hence, the external quantum efficiency (EQE) can be

determined by IPCE measurement. Moreover, the J_{sc} parameter is estimated after integrating all the photocurrent density values obtained from IPCE measurement since the values are plotted as a function of each wavelength[52].

$$\mathrm{IPCE}(\lambda) = \mathrm{EQE}(\lambda) = \frac{\mathrm{electrons}\,(\mathrm{cm^{-2}s^{-1}})}{\mathrm{photons}\,(\mathrm{cm^{-2}s^{-1}})} = \frac{|j_{ph}\,(\mathrm{mA/cm^2})| \times 1239.8\,(\mathrm{V\times nm})}{\mathrm{P_{mono}}\,(\mathrm{mW/cm^2}) \times \lambda} \quad (2)$$

The j_{ph} and P_{mono} indicate experimentally obtained photocurrent value and power intensity of monochromatic incident light of a particular wavelength λ, respectively.

To understand the enhancement of $J_{sc,}$ the electrochemical impedance spectroscopy (EIS) analysis was carried out as shown in Fig. 4-8C and 4-8D. In the Nyquist plot, the resistance value of the lowest point in the semicircle (near to 0 Ω) is related to the resistance of the both sides of electrodes (anode and cathode) and their interfaces[41,42]. In this study, we consider that the reduced resistance value at the lower resistance region resulted from the improved carrier conductance in the ITO/PEDOT:PSS, because there were no changes in the BHJ/cathode part[41,42]. The increased PEDOT-rich grains bring about improvement in the current paths and enhancement in the charge conductance[35-40]. Therefore, the hole transport performance of PEDOT:PSS layer with GQDs were improved due to the enhanced efficiency of the charge extraction from the BHJ layer, which resulted in the enhancement of J_{sc} parameter[45].

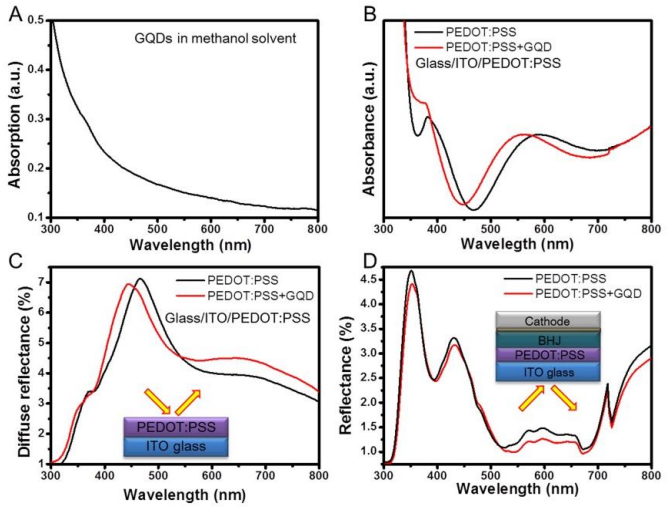

Figure 4-9. UV- visible adsorption spectra of GQDs in methanol solvent (A). UV-visible adsorption spectra (B) and diffuse reflectance spectra (C) of 40nm-thick PEDOT:PSS films coated on ITO glass. Reflectance spectra of full device structural samples (ITO/PEDOT:PSS/BHJ/TiO_x/Al) where from 700 nm to 750 nm is a lamp changing region (D). 0.4 wt % of GQDs were incorporated into PEDOT:PSS layer.

Although GQDs absorb visible region in the solar spectrum, the incorporation of GQDs hardly affects the transmittance of PEDOT:PSS layer. Fig. 4-9B shows the negligible changes in absorbance of PEDOT:PSS layer between w/o and w/ GQDs. The diffuse reflectance data of GQDs/PEDOT:PSS films is slightly enhanced at visible region above 550 nm of solar spectrum (Fig 4-9.). In addition, the incorporation of GQDs reduce the overall reflectance of OPV devices (ITO/PEDOT:PSS/BHJ/TiOx/Al) when the incident light is irradiated from the ITO glass side. This reveals that the incident light path from anode to BHJ layer was not disrupted when 0.4 wt % of GQDs were incorporated into the PEDOT:PSS layer. The IPCE data, in Fig. 4-8B, shows that the adding of GQDs in the PEDOT:PSS increased the IPCE values in the wavelength range of 300 nm to 800 nm. The IPCE

enhancement curve also displays that the increase of wavelength above 550 nm was slightly larger than at shorter wavelength, which results are well matched with the reflectance data in Fig. 4-9C and 4-9D. This suggests that the improved IPCE result is in reliance with the scattering effect. Unlike the conventional metal-nanoparticle-embedded PEDOT:PSS hole extraction layers, we could neglect the SPR effect on GQDs despite their large amount of electron density. From the calculated E-field intensity distribution of a single Au nanoparticle and GQD, considerable plasmonic effects in the PEDOT:PSS layer with GQDs were not observed (Fig 4-10.). Furthermore, the dramatically changed surface morphology of the GQDs-incorporated PEDOT:PSS elongates the incident light path in the device due to the relative index of GQDs (n=1.6 and k=0.02 at 600 nm of wavelength)[15-18,47]; this phenomenon is less dominant in the device compared to the morphological tuning effect of the PEDOT:PSS layer.

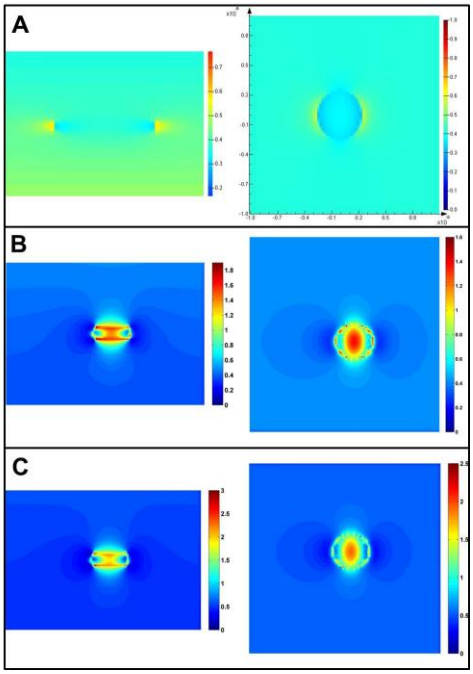

Figure 4-10. Optical simulation of E-field intensity distribution of GQD obtained by the finite difference time domain (FDTD) method at 500nm (A). (B) and (C) show optical simulation of a gold nanoparticle with the same shape and size as GQDs at 500nm and 600nm respectively.

Nevertheless the charge conductance and the light harvesting performance were improved with GQDs, the fill factor of GQDs in HTL device was slightly lower than the reference device. This is because of the unconformable energy levels of GQDs as shown in Fig 4-11. And slightly low R_{sh} value[43,44] in Table 4-2. However, this negative effect of GQDs can be overcome by improving the morphological characteristics of composite film, which was confirmed by comparing the dispersion of as-synthesized GQDs and hydrothermally deoxidized rGQDs in the PEDOT:PSS film (Fig. 4-12)[22].

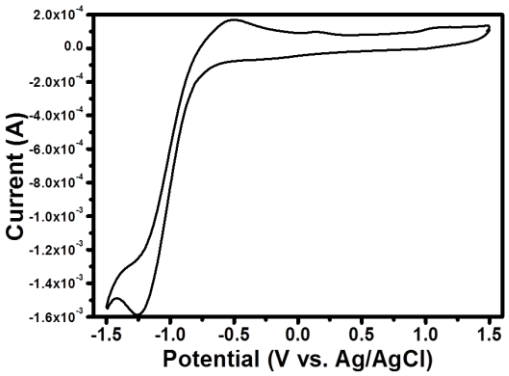

Figure 4-11. Cyclic voltammetry (CV) curves (scanning rate of 50 mV/s) of GQDs deposited on a platinum (Pt) sheet in acetonitrile solution with 0.1M tetrabutylammonium hexafluorophosphate as an electrolyte. Pt foil and Ag/AgCl were used as the counter and the reference electrodes. GQD solutions were drop-cast on the Pt sheet and fully dried to prepare the working electrode.

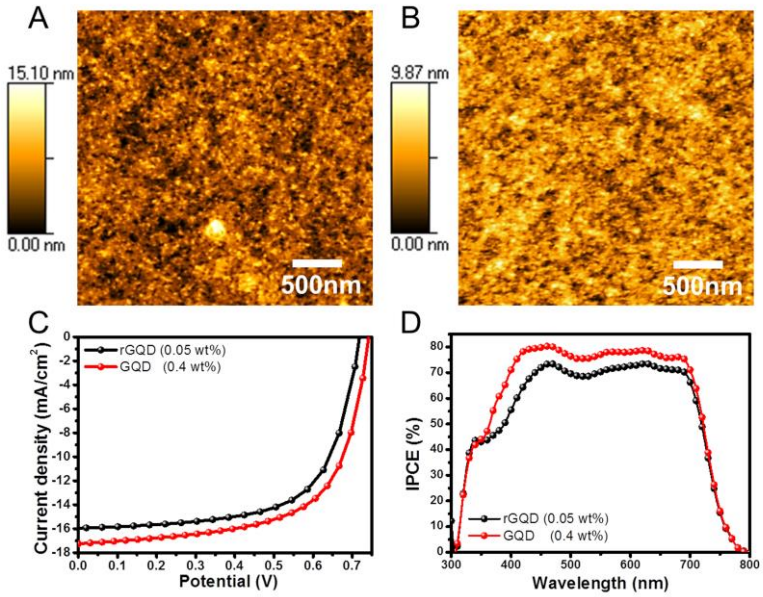

Figure 4-12. AFM and device performance in comparison with rGQD and GQDs in PEDOT:PSS. AFM images of PEDOT:PSS films incorporating 0.05 wt% of rGQDs (A) and 0.4 wt% of GQDs (B).Current vs. potential (J-V) curves (C), and incident photon-to-charge-carrier-efficiency (IPCE) (D) for the devices.

Previously, it was demonstrated that the oxygen-based moiety signals in XPS or FT-IR were strongly related to the quantitativeness of surface oxygen related functional groups of GQDs.

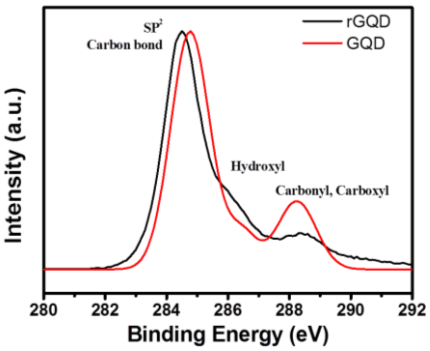

Figure 4-13. XPS C1s spectra of reduced GQDs (rGQD) and GQDs.

From XPS measurement in Fig 4-13, GQDs contain a much stronger oxygen-based moiety signals than rGQDs. The hydrothermal method caused preponderant sp^2 carbons in rGQDs so that the oxygen based functionalities of rGQDs were reduced. As shown in AFM images in Fig. 4-12A and 4-12B, even though the amount of rGQDs incorporated into PEDOT:PSS film was 20 times less than GQDs, the aggregated particles were much more observed on the surface of rGQDs-incorporated PEDOT:PSS film. As a result, the device performances might also strongly depend on the film quality of PEDOT:PSS layer as shown in Fig. 4-12. The rGQD incorporated device optimization information was described in Fig. 4-14 and 4-15.

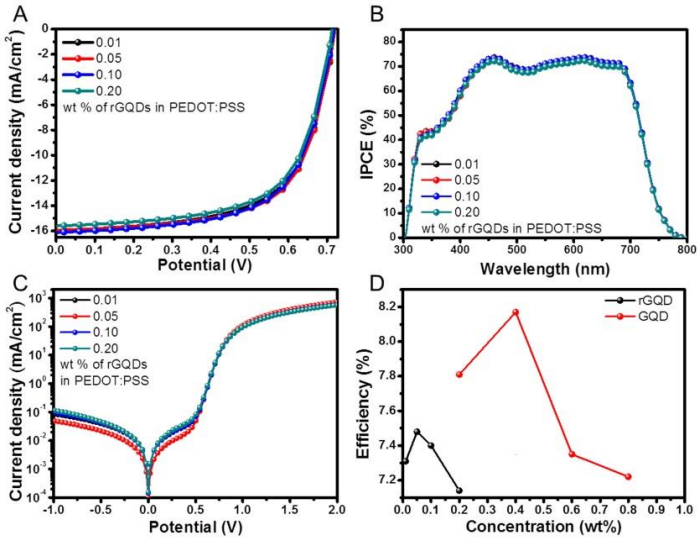

Figure 4-14. Current vs. potential (J-V) curves (A), incident photon-to-charge-carrier-efficiency (IPCE) (B) and dark current density-potential curves (C) of the devices with various rGQD concentrations in the PEDOT:PSS layer. Efficiency curves of OPV devices according to the GQDs or rGQDs concentration (D), where PEDOT:PSS films were prepared by incorporating rGQDs (black) and GQDs(red). Each point displays the average value of PCE at the concentration.

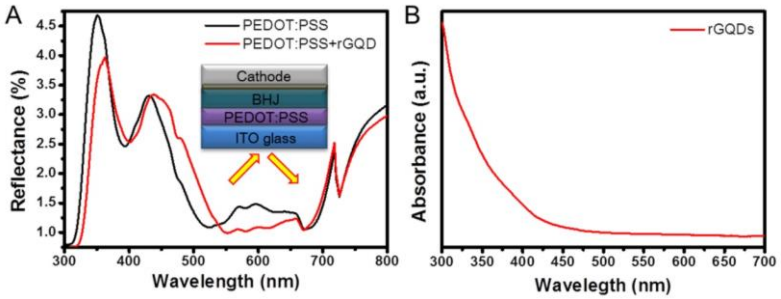

Figure 4-15. Reflectance spectra of full device structural samples (ITO/PEDOT:PSS/BHJ/TiO_x/Al) where from 700 nm to 750 nm is a lamp changing region, where 0.05 wt % of rGQDs were incorporated into the PEDOT:PSS layer (A). UV- visible adsorption spectra of rGQDs (B).

4.4. Synergistically improved PCE of the OPVs by incorporating GQDs into the polymer layers.

In our previous results, embedding the rGQDs in BHJ layers have enhanced the device performances of OPVs[22]. To take advantage of the synergistic effects, GQDs and rGQDs were placed in the PEDOT:PSS layer and the BHJ layer, respectively. Fig. 4-16A shows a schematic illustration of the device with the rGQDs-incorporated BHJ film, which was coated on the GQDs-incorporated PEDOT:PSS film. The PCE value of the device composed of the BHJ layer with rGQD and bare PEDOT:PSS (rGQDs in BHJ device) was increased by about 10 % as shown in Table 4-2. The FF was increased from 64.8 % for reference device to 71.8 % for rGQDs in BHJ device due to the improved carrier conductance and reduced resistance factors. The outstanding synergistic effects were observed in the device with the rGQDs-incorporated BHJ layer and the GQDs-incorporated PEDOT:PSS layer (GQD in PEDOT:PSS/rGQD in BHJ device), representing 8.67 % PCE, resulting in 13 % increase. The J_{sc} parameter was improved simultaneously with FF parameter. This result reveals that the positive effects from GQDs and rGQDs on the device educe the synergistic enhancement of the OPV performance without impeding each other.

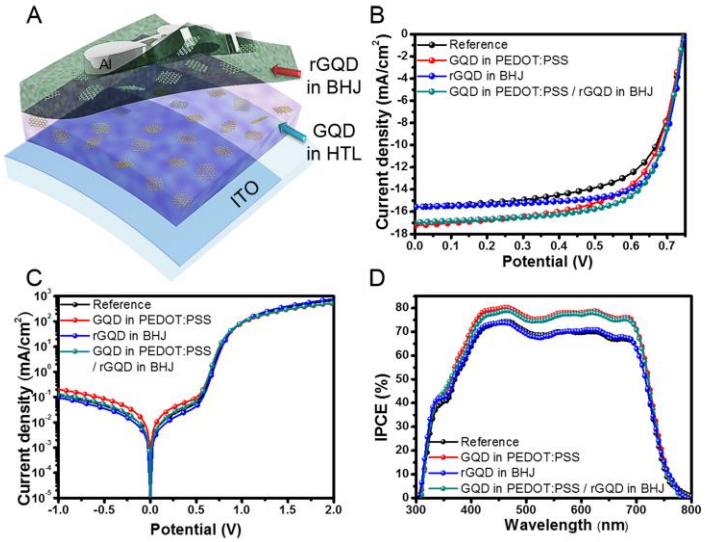

Figure 4-16. Device performance of rGQDs and GQDs incorporated OPVs. (A) Schematic illustration of the device with rGQDs in BHJ layer and GQDs in HTL (PEDOT:PSS), (B) J-V curves, (C) dark J-V curves and (D) IPCE of the devices with plain PEDOT:PSS and BHJ (black), PEDOT:PSS with GQDs (red), BHJ with rGQDs (blue) and GQDs and rGQDs incorporated PEDOT:PSS and BHJ (green). The concentration ratios of GQDs and rGQDs were 0.4 wt % and 0.02 wt % respectively.

In summary, the hydrophilic GQDs simply derived from carbon fibers were successfully incorporated into the PEDOT:PSS layer of an polymer BHJ photovoltaic device to enhance the power conversion efficiency. The high dispersibility of GQDs in polar solvents such as methanol allowed homogeneous incorporation of GQDs in hydrophilic PEDOT:PSS solution. The incorporation of GQDs with the sufficient oxygen based functionalities led to a significant morphological changes in PEDOT:PSS layer that improved the carrier conductance. Moreover, the GQDs-incorporation induced PEDOT:PSS layer extended light scattering and light confinement inside the OPV device. Taking these advantages of using GQDs in OPVs, the

J_{sc} value has been increased by 10 %. In addition to the incorporation of GQDs in the hole extraction layer, hydrophobic GQDs that were thermally reduced (rGQD) were hybridized in a bulk-heterojunction layer, which synergistically improved the PCE of OPV devices up to 8.67%.

Table 4-2. Performance parameters of the reference device with plain hole transporting layer (HTL, PEDOT:PSS), and the GQDs device composed of GQDs incorporated HTL and rGQD device composed of reduced GQDs incorporated HTL.

	V_{oc} (V)	J_{sc} (mA/cm^2)	FF (%)	PCE [a] (%)	R_{sh} [b] (KΩcm^2)
Reference	0.746 (±0.001)	15.6 (±0.01)	64.8 (±0.13)	7.52 (±0.08)	12.2
GQDs in HTL [c]	0.741 (±0.001)	17.3 (±0.03)	64.0 (±0.16)	8.17 (±0.08)	8.57
rGQDs in HTL [d]	0.719 (±0.012)	15.9 (±0.05)	65.4 (±0.21)	7.48 (±0.14)	18.8
rGQDs in BHJ [e]	0.748 (±0.002)	15.5 (±0.05)	71.8 (±0.20)	8.34 (±0.05)	17.4
GQDs in HTL/ rGQDs in BHJ	0.744 (±0.002)	16.9 (±0.08)	68.9 (±0.18)	8.67 (±0.10)	11.5

a)The device performance was average, as measured by six devices. To determine the cell area, the circular aperture (11.43 mm2) was used on top of the active area (15.71 mm2). b)The shunt resistance values were obtained by using a same calculation process with our previous report.46 c)The 0.4 wt.% of GQDs was incorporated into PEDOT:PSS. d)The 0.05 wt.% of rGQDs was incorporated into PEDOT:PSS. e)The 0.02 wt.% of rGQDs was incorporated into BHJ.

4.5. Methods

Synthesis of Graphene Quantum Dots and Reduced Graphene Quantum Dots. GQDs were synthesized by acidic treatments of carbon fiber with 20 ml of HNO_3 and 60 ml of H_2SO_4, and a thermal reaction at 120 ^oC[34]. After stirred for 24 hours, the mixture was diluted with 800 ml deionized water and neutralized by the addition of Na_2CO_3 to obtain a near pH 7. The reduced GQDs (rGQDs) were fabricated by using hydrothermal cutting methods from GOs.[22] The purified GOs, synthesized by the modified Hummer's method, were treated using thermal reduction at 250 ^oC for 2 h. The graphite powder was dissolved in an acid solution composed of sulphuric acid and nitric acid to oxidize. After mild sonication for 1 day and dilution in distilled water, the solution was centrifuged for 30 min at 4000 rpm. The rinsing process, dilution and centrifugation, were repeated six times and the rinsed RGO was hydrothermally reduced 200 ^oC for 10 h to fabricate the rGQDs. After the obtained GQDs and rGQDs solutions were filtered with a 20 nm porous anodisc, it were dialyzed for 3 days to obtain the purified GQDs and rGQDs using a 2000 Da dialysis bag, respectively. Finally, the GQDs were re-dispersed in the methanol solvent for incorporating into the PEDOT:PSS layer. In addition, before preparing the BHJ with rGQDs solution, the rGQDs was re-dispersed in the chlorobenzene solvent.

Fabrication of OPVs. The hole extraction layer was prepared by incorporating GQDs into PEDOT:PSS (AI4083, Clevious) solution with various weight

ratios. The total quantity of methanol used as a co-solvent was same in the all PEDOT:PSS solution. A 40 nm thick PEDOT:PSS layer was spin-cast on a pre-cleaned ITO glass and then dried at 150 ºC for 15 min. After that, an 80 nm thick layer of BHJ was spin-coated in an Ar filled glove box. The BHJ solution composed of PTB7 (1-Material Chemscitech Inc., Lot #:YY5220) and $PC_{71}BM$ (Nano-c) with 1:1.5 of weight ratio was prepared to 2.5 wt % in 3 % of 1,8-diiodooctane mixed chlorobenzene solvent. In the case of preparatory for devices with rGQDs/BHJ layer, 0.02 wt % of rGQDs was blended in the BHJ solution. Then, approximately 6 nm of TiOx interlayer was spin-coated for electron conducting layer and a 120 nm thick Aluminum metal cathode was deposited by thermal evaporation at ~10^{-7} Torr.

Characterization. The AFM images for GQDs were measured by noncontact mode with a Park System XE-100 atomic force microscope. The TEM images were obtained with a JEOL JEM-3010 electron microscope operating at 300 kV and Spherical aberration corrected transmission electron microscopy (Cs-corrected TEM) images were obtained with a JEOL JEM ARM 200F. In order to prepare the samples for TEM measurement, pre-formed PEDOT:PSS layer was stamping-transferred on a TEM grid by a dry-transfer method with a rigiflex polyurethane acrylate coated polycarbonate (PUA/PC) mold as previously reported method[45,48]. The FT-IR spectra were obtained by using a Thermo Scientific Nicolet 6700 spectrometer. XPS analysis was carried out with a Thermo Scientific K-Alpha small-spot X-ray Photoelectron Spectrometer (XPS) system. We prepare our GQD samples for FT-IR and

XPS measurements by using the same method with our previous report[22]. The surface topology images of PEDOT:PSS were investigated using atomic force microscopy (AFM, Dimension 3100, Veeco, Plainview, NY) in tapping mode. The absorption and reflectance were obtained using a UV-vis spectrophotometer (UV-3600, Shimadzu). The diffuse reflectance was measured using UV-vis spectrophotometer (Cary 5000) equipped with an integrating sphere accessory. The J-V device performances were measured by a solar simulator (Oriel 91193, 1000W lamp with 100mW/cm^2) using an NREL-calibrated Si solar cell and Keithley 2400 source meters. The incident photon-to-current efficiency (IPCE) measurements were performed by using a Solar Cell QE/IPCE Measurement (Zolix Solar Cell Scan 100).

4.6. References

1. Sariciftci, N. S.; Smilowitz, L.; Heeger, A. J.; Wudl, F. *Science*, **1992**, 258, 1474-1476.

2. Yu, G.; Gao, J.; Hummelen, J. C.; Wudl, F.; Heeger, A. J. *Science* **1995**, 270, 1789-1791.

3. Heeger, A. J. *Angew. Chem., Int. Ed.* **2001**, 40, 2591-2611.

4. Blom, P. W. M.; Mihailetchi, V. D.; Koster, L. J. A.; Markov, D. E. *Adv. Mater.* **2007**, 19, 1551-1566.

5. Markov, D. E.; Amsterdam, E.; Blom, P. W. M.; Sieval, A. B.; Hummelen, J. C. *J. Phys. Chem. A* **2005**, 109, 5266-5274.

6. Wang, D. H.; Moon, J. S.; Seifter, J.; Jo, J.; Park, J.H.; Park, O. O.; Heeger, A. J. *Nano Lett.* **2011**, 11, 3163-3168.

7. Hoven, C. V.; Dang, X.-D.; Coffin, R. C.; Peet, J.; Nguyen, T.Q.; Bazan, G. C. *Adv. Mater.* **2010**, 22, E63-E66.

8. Ma, W.; Yang, C.; Gong, X.; Lee, K.; Heeger, A. J. *Adv. Funct. Mater.* **2005**, 15, 1617-1622.

9. Brabec, C. J.; Sariciftci, N. S.; Hummelen, J. C. *Adv. Funct. Mater.* **2001**, 11, 15-26.

10. Wang, D. H.; Choi, D.-G.; Lee, K.-J.; Park, O. O.; Park, J. H. *Langmuir* **2010**, 26, 9584-9588.

11. Wang, D. H.; Choi, D.-G.; Lee, K.-j.; Im, S. H.; Park, O. O.; Park, J. H. *Org. Electron.* **2010**, 11, 1376-1380.

12. Atwater, H. A.; Polman, A. *Nat. Mater.* **2010**, 9, 205-213.

13. Wang, D. H.; Park, K. H.; Seo, J, H.; Seifter, J.; Jeon, J, H.; Kim, J. K.; Park, J. H.; Park, O. O.; Heeger, A. J. *Adv. Energy Mater.* **2011**, 1, 766-770.

14. Wang, D. H. Kim, D. Y.; Choi, K. W.; Seo, J. H.; Im, S. H.; Park, J. H.; Park, O. O.; Heeger, A. J. *Angew. Chem., Int. Ed.* **2011**, 50, 5519-5523.

15. Wang, D. H. Kim, J. K.; Lim, G.-H.; Park, K. H.; Park, O. O.; Park, J. H. *RSC Adv.* **2012**, 2, 7268-7272.

16. Lu, L.; Luo, Z.; Xu, T.; Yu, L. *Nano Lett.* **2012**, 13, 59-64.

17. Baek, S.-W.; Noh, J.; Lee, C.-H.; Kim, B.S.; Seo, M.-K.; Lee, J.-Y. *Sci. Rep.* **2013**. 3, 1726.

18. Ko, S.-J.; Choi, H.; Lee, W.; Kim, T.; Lee, B. R.; Jung, J.-W.; Jeong, J.-R.; Song, M. H.; Lee, J. C.; Woo, H. Y.; Kim, J. Y. *Energy Environ. Sci.* **2013**, 6, 1949-1955.

19. Xue, M.; Li, L.; Tremolet de Willers, B. J.; Shen, H.; Zhu, J.; Yu, Z.; Stieg, A. Z.; Pei, Q.; Schwarz, B. J.; Wang, K. L. *Appl. Phys. Lett.* **2011**, 98, 253302.

20. Janković, V.; Yang, Y.; You, J.; Dou, L.; Liu, Y.; Cheung, P.; Chang, J. P.; Yang, Y. *ACS Nano* **2013**, 7, 3815-3822.

21. Choi, H.; Lee, J.-P.; Ko, S.-J.; Jung, J.-W.; Park, H.; Yoo, S.; Park, O.; Jeong, J.-R.; Park, S.; Kim, J. Y. *Nano Lett*. **2013**, 13, 2204-2208.

22. Kim, J. K.; Park, M. J.; Kim, S. J.; Wanh, D. H.; Cho, S. P.; Bae, S.; Park, J. H.; Hong, B. H. *ACS Nano* **2013**, 7, 7207-7212.

23. Li, Y.; Zhao, Y.; Shi, Q.; Deng, L.; Hou, Y.; Qu, L. *Adv. Mater*. **2011**, 23, 776-780.

24. Gupta, V. Chaudhary, N.; Srivastava, R.; Sharma, G. D.; Bhardwaj, R.; Chand, S. *J. Am. Chem. Soc*. **2011**, 133, 9960-9963.

25. Shen, J.; Zhu, Y.; Yang, X.; Li, C. *Chem. Commun*. **2012**, 48, 3686-3699.

26. Wang, X.; Zhi, L.; Mullen, K. *Nano Lett*. **2008**, 8, 323-327.

27. Eda, G.; Fanchini, G.; Chhowalla, M. *Nat. Nanotechnol*. **2008**, 3, 270-274.

28. Robinson, J. T.; Perkins, F. K.; Snow, E. S.; Wei, Z.; Sheehan, P. E. *Nano Lett*. **2008**, 8, 3137-3140.

29. Robinson, J. T.; Zalalutdinov, M.; Baldwin, J. W.; Snow, E. S.; Wei, Z.; Sheehan, P.; Houston, B. H. *Nano Lett*. **2008**, 8, 3441-3445.

30. Eda, G.; Lin, Y.-Y.; Miller, S.; Chen, C.-W.; Su, W.-F.; Chhowalla, M. *Appl. Phys. Lett.* **2008**, 92, 233305.

31. Park, S.; Ruoff, R. S. *Nat. Nanotechnol*. **2009**, 4, 217-224.

32. Becerril, H. A.; Mao, j.; Liu, Z.; Stoltenberg, R. M.; Bao, Z.; Chen, Y. *ACS Nano* **2008**, 2, 463-470.

33. Zhu, Z.; Ma, J.; Wang, z.; Mu, C.; Fan, W.; Du, L.; Bai, Y.; Fan, L.; Yan, H.; Philips, D. L.; Yang, S. *J. Am. Chem. Soc.* **2014**, 136, 3760-3763.

34. Peng, J.; Gao, W.; Gupta, B. K.; Liu, Z.; Romero-Aburto, R.; Ge, L.; Song, L.; Alemany, L. B.; Zhan, X.; Gao, G.; Vithayathil, S. A.; Kaipparettu, B. A.; Marti, A. A.; Hayachi, T.; Zhu, J.-J.; Ajayan, P. M. *Nano Lett.* **2012**, 12, 844-849.

35. Sun, K.; Xia, Y.; Ouyang, J. *Sol. Energy Mater. Sol. Cells* **2012**, 97, 89-96.

36. Jönsson, S. K. M.; Birgerson, J.; Crispin, X.; Greczyski, G.; Osicowicz, W.; Denier van der Gon, A. W.; Salaneck, W. R.; Fahlman, M. *Synth. Met.* **2003**, 139, 1-10.

37. Nardes, A. M.; Janssen, R. A. J.; Kemerink, M. *Adv. Funct. Mater.* **2008**, 18, 865-871.

38. Ouyang, J.; Chu, C. W.; Chen, F. C.; Xu, Q.; Yang, Y. *Adv. Funct. Mater.* **2005**, 15, 203-208.

39. Kim, Y. H.; Sachse, C.; Machala, M. L.; May, C.; Müller-Meskamp, L.; Leo, K. *Adv. Funct. Mater.* **2011**, 21, 1076-1081.

40. Yeo, J. S.; Yun, J. M.; Kim, D. Y.; Kim, S. S.; Na, S. I. *Sol. Energy Mater. Sol. Cells* **2013**, 114, 104-109.

41. Zhou, H. Zhang, Y.; Seifter, J.; Collins, S. D.; Luo, C.; Bazan, G. C.; Nguyen, T.-Q.; Heeger, A. J. *Adv. Mater.* **2013**, 25, 1646-1652.

42. Leever, B. J.; Bailey, C. A.; Marks, T. J.; Hersam, M. C.; Durstock, M. F. *Adv. Energy Mater.* **2012**, 2, 120-128.

43. Lee, T. W.; Park, O. O.; Yoon, J.; Kim, J. J. *Adv. Mater*. **2001**, 13, 211-213.

44. Kim, J. K.; Park, H. S.; Rhee, D. K.; Ham, S.-J.; Lee, K.-J.; Yoo, P. J.; Park, J. H. *J. Mater. Chem.* **2012**, 22, 7718-7723.

45. Kim, J. K.; Park, I.; Kim, W.; Wang, D. H.; Choi, D.-G.; Choi, Y. S.; Park, J. H. *Chemsuschem* **2014**, 7, 1957-1963.

46. Wang, D. H.; Kim, J. K.; Seo, J. H.; Park, I.; Hong, B. H.; Park, J. H.; Heeger, A. J. *Angew. Chem. Int. Ed.* **2013**, 125, 2946-2952.

47. Kim, W.; Kim, N.; Kim, J. K.; Park, I.; Choi, Y. S.; Wang, D. H.; Chae, H.; Park, J. H. *ChemSusChem* **2013**, 6, 1070-1075.

48. Kim, J. K.; Veerappan, G.; Heo, N.; Wang, D. H.; Park, J. H. *J. Phys. Chem. C* **2014**, 118, 22672-22677.

49. Liu, H.; Goh, W.-P.; Leung, M.-Y.; Li, Y.; Norsten, T. B. *Sol. Energy Mater. Sol. Cells* **2012**, 96, 302.

50. Wu, B.; Wu, Z.; Guan, C.; Tai, K. f.; Yeow, E. K. L.; Fan, H. J.; Mathews, N.; Sum, T. C. *Nat. Commun.* **2013**, 4, 2004.

51. Lang, U., Müller, E., Naujoks, N. & Dual, J. Microscopical Investigations of PEDOT:PSS Thin Films. *Adv. Funct. Mater*. **19**, 1215 (2009).

52. Grätzel, M. Recent Advances in Sensitized Mesoscopic Solar Cells. *Acc. Chem. Res*. **42**, 1788 (2009).

Appendix

List of Publications

1. K. Choi, S. Nam, Y. Lee, M. Lee, J. Jang, S. J. Kim, Y. J. Jeong, H. Kim, S. Bae, J.-B. Yoo, S. M. Cho, J.-B. Choi, H. K. Chung, J.-H. Ahn, C. E. Park, and B. H. Hong, "**Reduced Water Vapor Transmission Rate of Graphene Gas Barrier Films for Flexible Organic Filed-Effect Transistors.**" ACS Nano, **2015**, 9, 5818-5824
2. S.J. Kim*, T. Choi*, B. Lee, S. Lee, K. Choi, J.B. Park, J.M. Yoo, Y.S. Choi, J. Ryu, P. Kim, J. Hone, B.H. Hong, "**Ultra-Clean Patterned Transfer of Single-Layer Graphene by Recyclable Pressure Sensitive Adhesive Films.**" *Nano Lett*., **2015**, 15, 3236-3240
3. D. Shin, J.B. Park, Y.-J. Kim, S.J. Kim, J.H. Kang, B. Lee, S.-P. Cho, B.H. Hong, K.S. Novoselov, "**Growth dynamics and gas transport mechanism of nanobubbles in graphene liquid cells.**" *Nat. Commun.* **2015**, 6, 6068
4. T. Choi*, S.J. Kim*(co-first authorship), S. Park, T.Y. Hwang, Y. Jeon, B.H. Hong, "**Roll-to-roll continuous patterning and transfer of graphene via dispersive adhesion.**" *Nanoscale*, **2015**, **7**, 7138-7142.
5. S.J. Kim*, K. Choi*, B. Lee, Y. Kim, B.H. Hong, "**Materials for Flexible, Stretchable Electronics: Graphene and 2D Materials.**" *Annu. Rev. Mater. Res*., 45, **2015**, 63-84
6. E. J. Lee, S. Y. Choi, H. Jeong, N. H. Park, W. Yim, M. H. Kim, J.-K. Park, S. Son, S. Bae, S. J. Kim, Y. H. Ahn, K. J. Ahn, B. H. Hong, J.-Y. Park, F. Rotermund, D.-I. Yeom, "**Active control of all-fibre graphene devices with electrical gating.**" *Nat. Commun*. **2015**, 6 (6851), 1-6.

7. M. Choi, J. Son, H. Choi, H.-J. Shin, S. Lee, S. Kim, S. Lee, S. Kim, K.-R. Lee, S.J. Kim, B.H. Hong, J. Hong, I.-S. Yang, "**In-situ Raman spectroscopy of current-carrying graphene microbridge.**" *J. Raman Spectrosc.*, **2014**, 25(2), 168-172.
8. N. W. Kim, J. Y. Kim, C. Lee, S.J. Kim, B. H. Hong, E.J. Choi, "**Infrared spectroscopy of large scale single layer graphene on self assembled organic monolayer.**" *Appl. Phys. Lett.*, **2014**, 104, 041904.
9. S.J. Kim*, J. Ryu*, S. Son, J.M. Yoo, J.B. Park, D. Won, E.-K. Lee, S.-P. Cho, S. Bae, S. Cho, B.H. Hong, "**Simultaneous Etching and Doping by Cu-Stabilizing Agent for High-Performance Graphene-Based Transparent Electrode**s." *Chem. Mater.*, **2014**, 26 (7), 2332-2336.
10. D.H. Wang, J.K. Kim, S.J. Kim, B. H. Hong, J.H. Park, "**Efficient solution-processed small-molecule solar cells by insertion of graphene quantum dots.**" *Nanoscale*, **2014**, 6, 15175-15180
11. J.K. Kim, M.J. Park, S.J. Kim, D.H. Wang, S.P. Cho, S. Bae, J.H. Park, B.H. Hong, "**Balancing Light Absorptivity and Carrier Conductivity of Graphene Quantum Dots for High-Efficiency Bulk Heterojunction Solar Cells.**" *ACS Nano* **2013**, 7 (8), 7207-7212.
12. J. Ryu, Y. Kim, D. Won, N. Kim, J.S. Park, E.-K. Lee, D. Cho, S.-P. Cho, S.J. Kim, G.H. Ryu, H.-A.S. Shin, Z. Lee, B.H. Hong, S. Cho, "**Fast Synthesis of High-Performance Graphene Films by Hydrogen-Free Rapid Thermal Chemical Vapor Deposition.**" *ACS Nano*, **2013**, 8 (1), 950-956.
13. J.Y. Kim, C. Lee, S. Bae, S. J. Kim, K. S. Kim, B. H. Hong, and E. J. Choi, "**Effect of uni-axial strain on THz/far-infrared response of graphene**". *Appl. Phys. Lett.* **2012,** 100, 041910
14. Y. J. Kim*, S. J. Kim*(co-first authorship)**,** M. H. Jung, K. Y. Choi, S. Bae, S.K. Lee, Y. Lee, D. Shin, B. Lee, H. Shin, M. Choi, K. Park, J.H. Ahn and B. H. Hong, "**Low-temperature growth and direct transfer of graphene–graphitic carbon films on flexible plastic substrates**." *Nanotechnology* **2012,** 23 344017.

15. S, Bae, S. J. Kim, D. Shin, J. H. Ahn, and B. H. Hong, "**Towards industrial applications of graphene electrodes**." *Phys. Scr*. **2012,** T146, 014024
16. J.Y. Kim, J. H. Rho, C. Lee, S. Bae, S. J. Kim, K. S. Kim, B. H. Hong, E. J. Choi," **Infrared Conductivity and Carrier Mobility of Large Scale Graphene on Various Substrates**." *J. Nanosci. Nanotechnol.* , **2012,** 12 (7), 5816-5819.

List of Presentations

International conferences

1. **S. J. Kim**, B. Lee, S. Lee, K. Choi, J. Park, J. M. Yoo, S. Kang, P. Kim, J. Hone, B. H. Hong, "Ultra-Clean Dry Transfer and Patterning of Graphene Films by Pressure Sensitive Adhesives" 1st IC2DMAT 2014, 2014(10) Hangzhou, China, (Poster)
2. **S. J. Kim**, J. Ryu, S. Son, D. Won, E.-K.Lee, S.-P. Cho, S. Bae, S.Cho, B. H. Hong, "Simultaneous Cu Etching and Doping of Graphene by Chelating Agent for High-Performance Transparent Electrodes" MRS Spring 2014, 2014 (04), San Francisco, USA, (Poster)
3. J. Son, M. Choi, **S. J. Kim**, S. Lee, S. Bae, S. Kim, S. Lee, B. H. Hong, I. Yang, J. Hong, "In-situ Raman study on CVD-grown graphene microbridge under high current density" Graphene 2012, 2012(04), Brussels, Belgium, (Poster)
4. **S. J. Kim**, Y.J. Kim, M. H. Jung, S. Bae, S.K. Lee, Y. Lee, D. Shin, B. Lee, H. Shin, M. Choi, K. Park, J.H. Ahn, and B. H. Hong "Low-Temperature Growth and Direct Transfer of Graphitic Carbon Films on Flexible Plastic Substrates" Nano Korea 2012 Symposium 2012(08), Seoul, Korea, (Poster)
5. **S. J. Kim**, S. Park, M. H. Jung, S. Bae, H. Jang, Y. Lee, J. -H. Ahn and B. H. Hong, "Low-temperature Transfer-free Graphene Growth

on Flexible Polymer Substrates.” Nano Korea 2011(8), Ilsan, Korea, (Poster)

6. **S. J. Kim**, J. Cha, S. Bae, D. Y. Jung, B. H. Hong “Graphene-Based Si and CIGS Solar Cells” RAGRM, 2010(8), Singapore, (Poster)

요약 (국문초록)

1장에서 플렉시블 전자소자, 광소자, 전기화학 에너지 저장 소자와 같은 미래 전자 소자의 재료로 각광받고 있는 2차원 물질에 대하여 간단히 소개한다. 그래핀, 보론나이트라이드, 칼코제나이드 전이금속 등 특성이 우수한 대표적인 2차원 물질들 중, 그래핀은 높은 전하이동도, 열전도도, 비면적, 투명도, 기계적 특성 및 환경안정성 등의 우수한 특성을 가지고 있어 플렉시블 전자소자 분야에서의 연구가 두드러진다.

대면적 그래핀의 생산을 위해서 화학기상증착법을 이용하여 합성된 그래핀의 구리 촉매의 식각 공정에 대한 연구가 중요하다. 2장에서 이온화된 구리 이온과 화합물을 만들 수 있는 벤지이미다졸 (BI)을 식각 용액에 첨가하고, 식각-도핑 동시 공정을 소개한다. 구리 안정제가 첨가된 식각 용액으로 처리된 그래핀은 추가적인 도핑 공정 없이 강한 도핑 효과에 의해 낮은 면저항 특성을 보여준다. 또한 이러한 강한 도핑 효과는 그래핀의 방지막 특성으로 인해, 상온 상압의 조건에서도 10개월 정도의 시간이 흘러도 유지되는 특성을 확인할 수 있다.

3장에서 압력 민감 접착제를 이용하여 그래핀의 표면이 이물질이 거의 남지 않고, 단가 경쟁에서 유리하며 쉽게 대면적이 가능한 전사 및 패터닝 공정에 대해 소개한다. 압력 민감 접착필름을 이용한 그래핀 전사는 젖음성 및 접착에너지의 차이를 이용하여 그래핀이 목표 기판으로 쉽게 이동하도록 한다. 이 공정을 이용하여 전사된 그래핀은 일반적인 다른 고분자 물질을 이용하여 전사된 그래핀에 비해 표면에 이물질이 적고, 상대적으로 도핑 효과가 적어 높은 전하이동도를 가지는 특성을 보인다. 또한, 압력 민감 접착필름은 4번 재사용하여 전사 공정에 사용하더라도 면저항 특성에 큰 영향을 미치지 않은 것을 확인할 수 있다.

4장에서는 광학적, 전기적 특성의 조절이 용이한 0차원 물질인 그래핀 양자점의 유기전자소자에 응용한 연구를 소개한다. 그래핀 양자점은 화학적 기능화 공정을 통해 분산도의 조절이 가능하다. 기능화 처리된 그래핀 양자점을 정공포집 고분자층에 적용한 태양전지 소자는 단락 회로 전류 밀도의 증가를 초래하고 소자의 전력변환효율이 향상되는 특성을 보인다. 또한, 환원된 그래핀 양자점을 벌크 이종접합에 삽입하는 공정을 추가하여 그래핀 양자점이 적용된 유기태양전지의 효

율 향상에 대한 시너지 효과를 관찰한다.

주요어: 그래핀, 그래핀 양자점, 화학적 도핑, 압력민감점착필름, 투명전극, 유기태양전지

학번: 2012-30871